# **Supporting Information**

# High-Performance Dendrite-Free Lithium Textile Anodes Using Interfacial Interaction-Mediated Ultrathin Metal Organic Framework Multilayers

Donghyeon Nam<sup>1,3</sup>, Gwonho Yu<sup>2</sup>, Chanseok Lee<sup>1</sup>, Jeongyeon Ahn<sup>1</sup>, Boyeon Kim<sup>1</sup>, Sungha Choi<sup>1</sup>, Keun Hee Kim<sup>3</sup>, Donghyeok Roh<sup>3</sup>, Hyewon Kang<sup>3</sup>, Jeong Gon Son<sup>2,4</sup>, Hyung-Jun Koo<sup>5</sup>, Jieun Lee<sup>6</sup>, Seoin Back<sup>2,7\*</sup>, Seung Woo Lee<sup>3\*</sup>, Yongmin Ko<sup>8\*</sup>, and Jinhan Cho<sup>1,2\*</sup>

<sup>1</sup>D. Nam, C. Lee, J. Ahn, B. Kim, S. Choi, Prof. J. Cho

Department of Chemical and Biological Engineering, Korea University, 145 Anam-ro, Seongbuk-gu, Seoul 02841, Republic of Korea

E-mail: jinhan71@korea.ac.kr

<sup>2</sup>G.Yu, Prof. S. Back, Prof. J. G. Son, Prof. J. Cho

KU-KIST Graduate School of Converging Science and Technology, Korea University, 145 Anam-ro, Seongbuk-gu, Seoul 02841, Republic of Korea

E-mail: sback@korea.ac.kr, jinhan71@korea.ac.kr

<sup>3</sup>D. Nam, K. H. Kim, D. Roh, H. Kang, Prof. S. W. Lee

The George W. Woodruff School of Mechanical Engineering, Georgia Institute of Technology, Atlanta, Georgia 30332, USA

E-mail: seung.lee@me.gatech.edu

<sup>4</sup>Prof. J. G. Son

Soft Hybrid Materials Research Center, Korea Institute of Science and Technology (KIST), 5 Hwarang-ro 14-gil, Seongbuk-gu, Seoul 02792, Republic of Korea

<sup>5</sup>Prof. H.-J. Koo

Department of Chemical & Biomolecular Engineering, Seoul National University of Science and Technology, 232 Gongneung-ro, Nowon-gu, Seoul 01811, Republic of Korea

<sup>6</sup>J. Lee

Energy Storage Research Center, Korea Institute of Science and Technology (KIST), 5 Hwarang-ro 14-gil, Seongbuk-gu, Seoul 02792, Republic of Korea

<sup>7</sup>Prof. S. Back

Department of Integrative Energy Engineering, Korea University, 145 Anam-ro, Seongbuk-gu, Seoul 02841, Republic of Korea

E-mail: sback@korea.ac.kr

<sup>8</sup>Y. Ko

Division of Energy & Environmental Technology, Materials Research Institute, Daegu Gyeongbuk Institute of Science and Technology (DGIST), 333 Techno Jungang-daero, Hyeonpung-eup, Dalseong-gun, Daegu 42988, Republic of Korea

E-mail: yongmin.ko@dgist.ac.kr

#### **Experimental Details**

*Materials:* All chemical reagents used in this study were purchased from Sigma–Aldrich and used without further purification. Organic solvents, including toluene and ethanol, were obtained from Daejung Chemicals & Metals Co., Ltd. (Republic of Korea).

Synthesis of TOA-Ag NPs: Tetra(octylammonium thiosulfate) (TOA)-stabilized Ag NPs dispersed in toluene were synthesized using a modified Brust–Schiffrin method<sup>[S1]</sup>. Briefly, 0.9 mmol of silver nitrate (AgNO<sub>3</sub>) in 24 mL of deionized water and 2.25 mmol of tetraoctylammonium bromide (TOABr) in 24 mL of toluene were added to a reaction flask and stirred for 10 minutes at room temperature. Subsequently, 3.6 mmol of sodium thiosulfate (Na<sub>2</sub>S<sub>2</sub>O<sub>3</sub>) was introduced into the mixture, resulting in the transformation of the initially cloudy solution into a clear, transparent phase. After stirring for an additional 10 min, the toluene phase—now containing the Ag precursor ions (Ag<sup>+</sup>)—was separated and transferred to a new flask.

To initiate reduction, 1.35 mmol of sodium borohydride (NaBH<sub>4</sub>) dissolved in 24 mL of deionized water was added dropwise to the toluene phase. Upon addition, the color of the solution immediately turned deep brown, indicating the formation of Ag NPs. The resulting mixture was vigorously stirred for 10 minutes. The deep brown-colored toluene phase was then isolated and sequentially washed with deionized water, 10 mmol L<sup>-1</sup> HCl, and 10 mmol L<sup>-1</sup> NaOH using a separating funnel. Larger Ag NPs were removed by centrifugation at 8,000 rpm for 10 minutes at 20 °C. The final TOA–Ag NPs obtained had an average diameter of approximately 8.3 nm.

LbL-assembly of (TOA-Ag NP/TREN)<sub>n</sub> multilayers: Si wafers (for FE-SEM), quartz glass (for UV-vis spectroscopy), and gold-sputtered Si wafers (for FTIR analysis were pretreated with UV irradiation ( $\lambda \sim 350$  nm) for 10 min to enhance surface reactivity prior to

multilayer deposition. Ni-electroplated polyester textiles, which readily interact with amine groups, were used without UV irradiation or chemical treatments. Si wafers (for FE-SEM), quartz glass (for UV–vis spectroscopy), gold-sputtered Si wafers (for FTIR analysis), and Ni-electroplated polyester textile substrates were immersed in a 1 mg mL<sup>-1</sup> ethanolic solution of branched poly(ethylene imine) (PEI) for 30 min, followed by rinsing twice with pure ethanol and drying under a gentle stream of air.

The PEI-modified substrates were subsequently immersed in a toluene solution of TOA–Ag NPs (10 mg mL<sup>-1</sup>) for 60 min, rinsed with pure toluene, and dried. Following this, the substrates were immersed in an ethanolic solution of tris(2-aminoethyl)amine (TREN, 1 mg mL<sup>-1</sup>) for 20 min, rinsed with pure ethanol, and dried thoroughly. These two dipping steps—TOA–Ag NP adsorption and TREN binding—were repeated alternately until the desired number of bilayers was achieved.

LbL-assembly of  $(Ag^+/TCA)_n$  multilayers: Si wafers (for FE-SEM) and quartz glass (for UV–vis spectroscopy) were also exposed to UV light ( $\lambda \sim 350$  nm) for 10 min before multilayer assembly and Ni-electroplated textiles were used without UV irradiation or chemical treatments. The substrates were treated with a 1 mg mL<sup>-1</sup> PEI solution in ethanol for 10 minutes, washed twice with pure ethanol, and dried under a stream of air. The PEI-coated substrates were then immersed in 1 mg mL<sup>-1</sup> PAA solution in ethanol for 10 minutes. These dipping cycles were repeated for 3 cycles. Then, the [PEI/PAA]<sub>3</sub>-coated substrates were dipped into an aqueous Ag<sub>2</sub>CO<sub>3</sub> solution (5 mg mL<sup>-1</sup>) for 10 min, rinsed thoroughly with deionized water, and dried. Subsequently, the substrates were immersed in an ethanol solution of trithiocyanuric acid (TCA, 2 mg mL<sup>-1</sup>) for 10 min. These alternating dipping steps were repeated to obtain the targeted number of bilayers.

Cell Assembly and Electrochemical Measurements: Electrochemical tests were conducted using CR2032-type coin cells (MTI Corporation), WBCS3000 multichannel workstation, and Arbin battery tester. All cell assembly procedures were carried out in an argon-filled glovebox (MBraun; O<sub>2</sub> < 0.1 ppm, H<sub>2</sub>O < 0.1 ppm). The fabricated textile anode (5-MOF-Ni-ET) possesses a total thickness of approximately 140 µm (after calendaring for cell assembly) and a total mass of 40 mg cm<sup>-2</sup>. Within this configuration, the amount of plated lithium was calculated based on the total charge passed during lithium deposition at 4 mAh cm<sup>-2</sup>. This corresponds to a lithium mass of ~1.04 mg cm<sup>-2</sup>, accounting for only 2.6 wt% of the total anode composite (textile host + lithium). Lithium chip (250 um-thick) and 20 µmthick lithium-coated copper foil were used as the anode, paired with the prepared cathode and glass fiber as the separator, depending on the cell configuration. For Li//n-MOF-Ni-ET halfcells, Li-n-MOF-Ni-ET//Li-n-MOF-Ni-ET symmetric cells, and Li-5-MOF-Ni-ET//LiFePO4 (LFP) full cells, the electrolyte consisted of 1 M lithium bis(trifluoromethanesulfonyl)imide (LiTFSI) in a 1:1 (v/v) mixture of 1,2-dimethoxyethane (DME) and 1,3-dioxolane (DOL), supplemented with 5 wt% lithium nitrate (LiNO<sub>3</sub>). For all coin cell, the electrolyte volume was fixed at 100 µL. Galvanostatic charge-discharge measurements for the full cells were performed within a voltage window of 3.5–4.0 V at a rate of 0.1 C during the initial two cycles. The theoretical specific capacity of LFP, used to calculate the C-rate, was set at approximately 170 mAh g<sup>-1</sup>. Electrochemical impedance spectroscopy (EIS) was carried out in the frequency range of 100 kHz to 0.1 Hz with a sinusoidal amplitude of 10 mV. All electrochemical experiments were conducted at room temperature (25 °C).

**Pouch Cell Assembly:** Pouch cells were fabricated inside the same argon-filled glovebox (MBraun;  $O_2 < 0.1$  ppm,  $H_2O < 0.1$  ppm). The aluminum and nickel tabs of the cathode and anode, respectively, were welded using an ultrasonic welder (GN-800, Gelon). The cell was then assembled by stacking a 20  $\mu$ m-thick lithium-coated copper foil (Cu foil: 11

μm thick), separator, and the prepared cathode inside a laminated pouch. After the electrolyte injection, the pouch cell was sealed under vacuum to complete the assembly process.

Characterization: The morphology and crystallinity of the nanoparticles were characterized using high-resolution transmission electron microscopy (HR-TEM, Tecnai 20, FEI). X-ray diffraction (XRD) patterns were collected using a Rigaku XRD-2500/PC with Cu Kα radiation (40 kV, 150 mA). Field-emission scanning electron microscopy (FE-SEM, S-4800, HITACHI) was employed to investigate the surface morphology, cross-sectional film thickness, and elemental composition via energy-dispersive X-ray spectroscopy (EDS). Fourier transform infrared (FTIR) spectra of multilayers deposited on gold-sputtered Si wafers were acquired in specular reflection mode using a CARY 600 (Agilent Technologies) at room temperature. Raw spectra were baseline-corrected and smoothed using OMNIC 9 software (Thermo Scientific). UV–vis absorption spectra of multilayers on quartz glass substrates were recorded using a Lambda 35 spectrophotometer (Perkin Elmer) across a wavelength range of 200–800 nm. The sheet resistance was measured by the four-point probe method using a Loresta-GP MCP-T610 (MITSUBISHI CHEMICAL ANALYTECH). Electrical conductivity was then calculated based on the measured sheet resistance and the film thickness determined from cross-sectional FE-SEM images.

Computational Details: Spin-polarized density functional theory (DFT) calculations were conducted using the Vienna Ab Initio Simulation Package (VASP) code version 5.4.4. [S2,S3] The projector augmented wave (PAW) pseudopotential method and the Perdew-Burke-Ernzehof (PBE) exchange-correlation functional were used. [S5,S6] The van der Waals interactions were described using Grimme's D3 method. [S7] The kinetic energy cutoff was set to 400 eV, and (2×4×1) and (3×3×1) gamma-point centered k-point grids were sampled for Ni and KGF-7 surface, respectively. [S8] The convergence tolerance of energy and force was set to

10<sup>-4</sup> eV and 0.05 eVÅ<sup>-1</sup>, respectively.

To simulate charged and discharged systems, we employed the grand-canonical DFT (GC-DFT) method.<sup>[S9]</sup> The electrolyte environment was represented as a polarizable continuum using the linearized Poisson-Boltzmann implicit solvation method, as implemented in VASPsol.<sup>[S10,S11]</sup> A dielectric constant of 7.17 was used to describe a 1:1 molar mixture of DOL and DME, and a Debye length of 3 Å was set to simulate a 1 M condition.<sup>[S12,S13]</sup>

In GC-DFT simulations, the potential of the studied system is varied by charging the unit cell, i.e., adding or removing electrons from the initial neutral system. The electrode potential versus the Li electrode ( $U_{Li}$ ) is linked to the chemical potential of an electron, with  $U_{Li} = -(\mu_e + 1.39 \text{ eV})/e$ , where 1.39 eV is the work function of the Li metal. [S14] The calculated DFT electronic energies were converted into GC-DFT energies by subtracting the product of  $\Delta n$  and the sum of  $\mu_e$  and  $V_{bulk}$ , the electrostatic potential of the bulk solvent, i.e.,  $E_{GC-DFT} = E_{DFT} - \Delta n(\mu_e + V_{bulk})$ . The positive (negative)  $\Delta n$  indicates the number of electrons added to (subtracted from) the system. Here,  $\mu_e$  represents the electron chemical potential, and  $V_{bulk}$  represents the electrostatic potential of the bulk solvent. Finally, the values of  $U_{Li}$  and  $E_{GC-DFT}$  were fitted to a quadratic equation to predict the GC-DFT energy as a function of the potential.

Structure Modeling: To simulate two distinct systems, we modeled the Ni (111) surface and the [Ag<sup>+</sup>/TCA]<sub>n</sub>-MOF (001) surface. The [Ag<sup>+</sup>/TCA]<sub>n</sub>-MOF structure was obtained from the Cambridge Crystallographic Data Centre (CCDC) with CCDC id of 2052284 (**Figure S12**). Considering the structural configuration of the [Ag+/TCA]<sub>n</sub>-MOF multilayers with TCA as the outermost layer, we constructed a TCA-terminated structure with the bottom layer of Ag, which was fixed during the optimization process. [S16]

**Adsorption Energy Calculation:** The adsorption energies of DME, DOL, NO<sub>3</sub><sup>-</sup>, and TFSI<sup>-</sup> were calculated as follows:

$$\Delta E_{ads} = E_{m \ obcub} * - E_{m \ obcub} - E_*$$

where,  $E_*$ ,  $E_{m \ obcub}$  \* and  $E_{m \ obcub}$  correspond to the DFT energies of the bare electrode surface, the molecule-adsorbed surface, and the isolated molecule in the  $15 \times 15 \times 15 \ \text{Å}^3$  cell, respectively. For anionic molecules, their charges were accounted for by adding an extra electron when calculating their molecular energies in the  $15 \times 15 \times 15 \ \text{Å}^3$  cell. Physical adsorption was considered by maintaining an appropriate distance from the surface, as the molecule acts as a solvent. Additionally, when anions adsorbed on the surface, their charges were compensated by placing a fixed Li<sup>+</sup> counterion in the same position within the vacuum region.

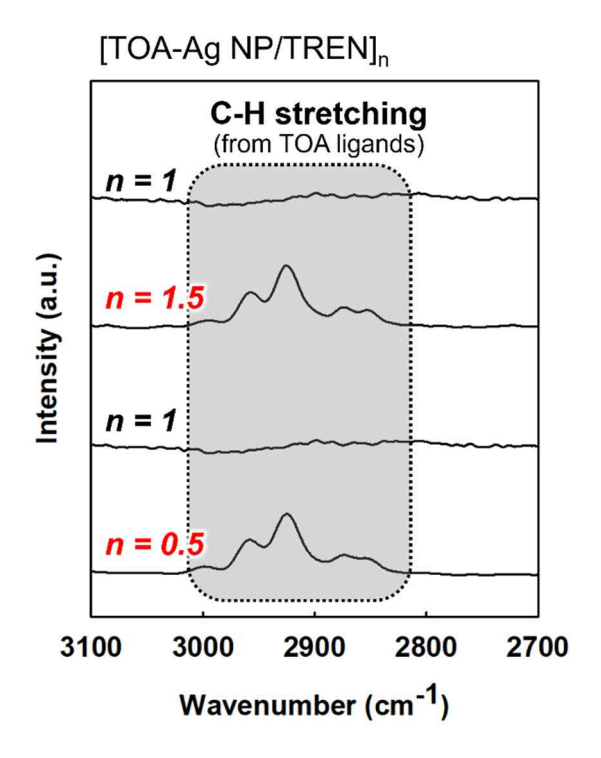


**Figure S1.** FTIR spectra of ligand-exchange LbL-assembled (TOA-Ag NP/TREN)<sub>n</sub> multilayers, with the bilayer number (n) increasing from 0 to 2. Initially, after immersing the poly(ethylene imine) (PEI)-coated substrate into a toluene solution of dispersed TOA-Ag NPs, the absorption peaks between approximately 2850-2950 cm<sup>-1</sup> indicate C-H stretching from the bulky TOA alkyl chains, confirming the deposition of the TOA-Ag NP layer (n = 0.5). These peaks diminish entirely after the substrate, now coated with the TOA-Ag NP layer, is immersed into an ethanol solution of dissolved TREN (n = 1), signifying the complete removal of TOA ligands from the Ag NP surface. Given that the NH<sub>2</sub> groups of TREN have a stronger affinity for the metal surface than the ammonium groups of TOA ligands, the FTIR spectra suggest a successful direct adsorption of TREN onto the Ag NP surface through an efficient ligand-exchange reaction. This pattern is consistently observed with subsequent layer, demonstrating the ligand exchange LbL assembly of the (TOA-Ag NP/TREN)<sub>n</sub> multilayers.

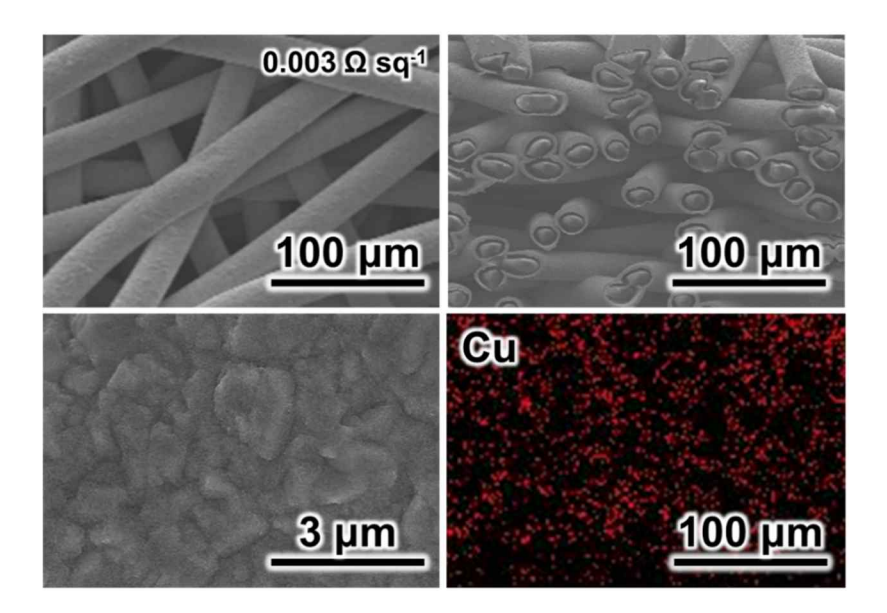


**Figure S2.** FE-SEM images and corresponding EDS elemental mapping of Cu-electroplated textile (Cu-ET). The formed Cu-ETs exhibited uniform Cu deposition across the entire textile surface while retaining the porous structure, similar to that observed in the Ni-ETs. The sheet resistance was measured to be  $0.003~\Omega~\text{sq}^{-1}$ .

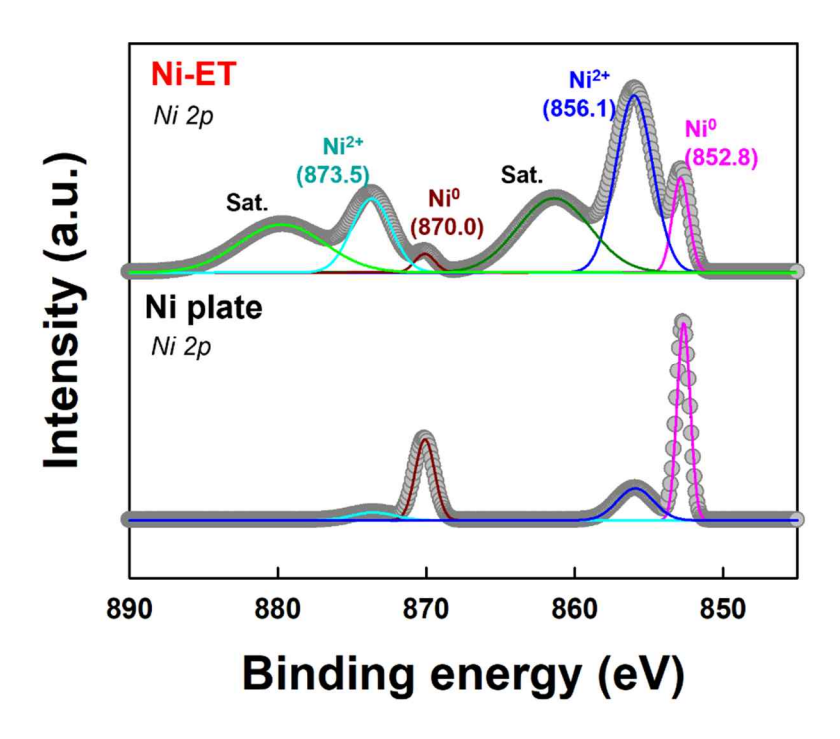


**Figure S3.** Ni 2p XPS spectra of the Ni-ET and the commercial Ni plate. Unlike the bulk Ni plate, which displays two strong peaks at 852.8 and 870.0 eV for metallic Ni<sup>0</sup> without noticeable satellites, the Ni-ET exhibited slightly broadened peaks at 856.1 and 873.5 eV for Ni<sup>2+</sup> with strong satellite features. The deconvolution of the Ni 2p spectrum revealed the presence of both  $\alpha$ -Ni(OH)<sub>2</sub> and  $\beta$ -Ni(OH)<sub>2</sub> phases.

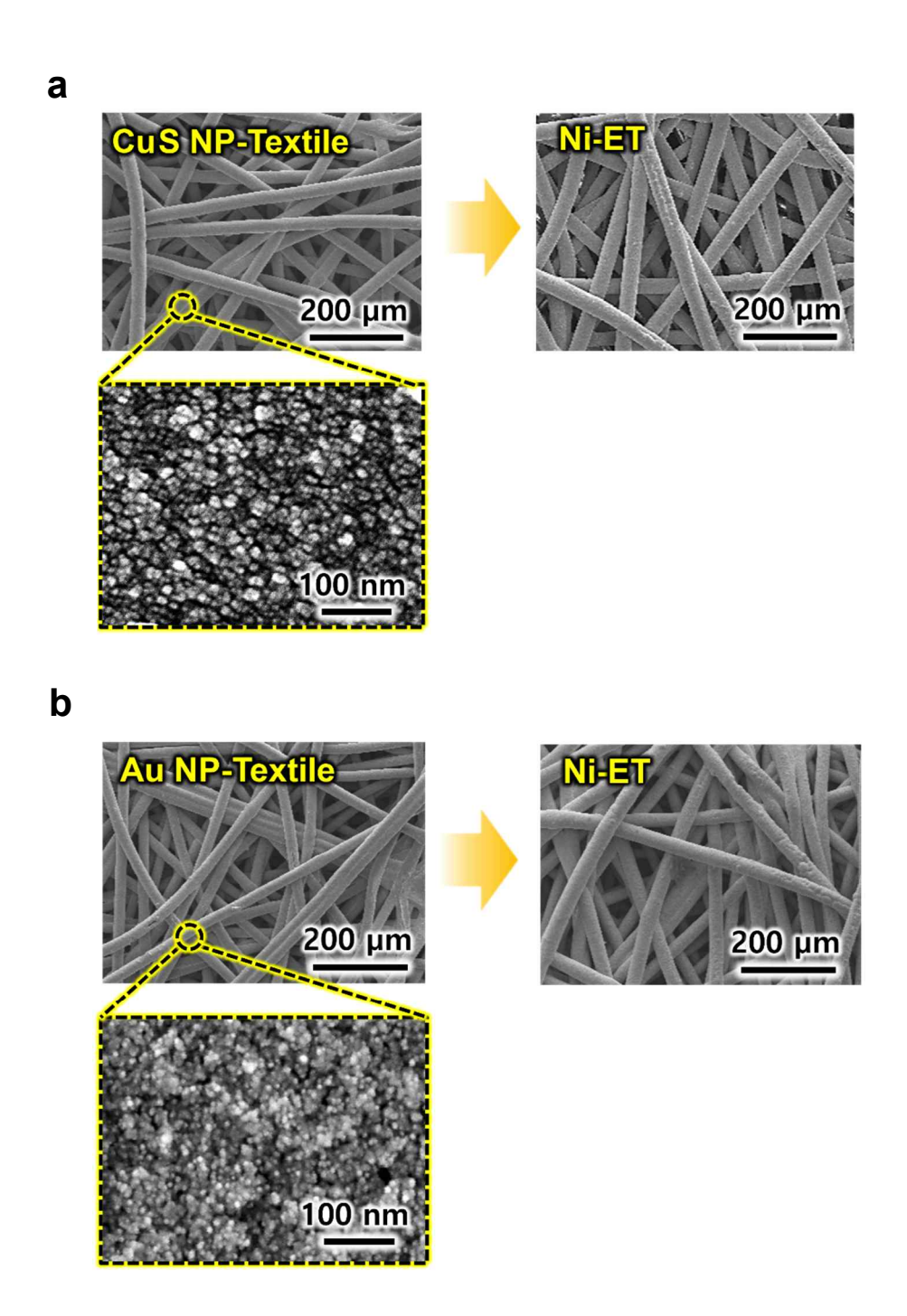


**Figure S4.** SEM images of (a) (TOA-CuS NP/cysteamine)<sub>n</sub> and (b) (TOA Au NP/TREN)<sub>n</sub> multilayer-coated polyester textiles, along with the corresponding Ni-ETs after Ni electroplating on each textile.

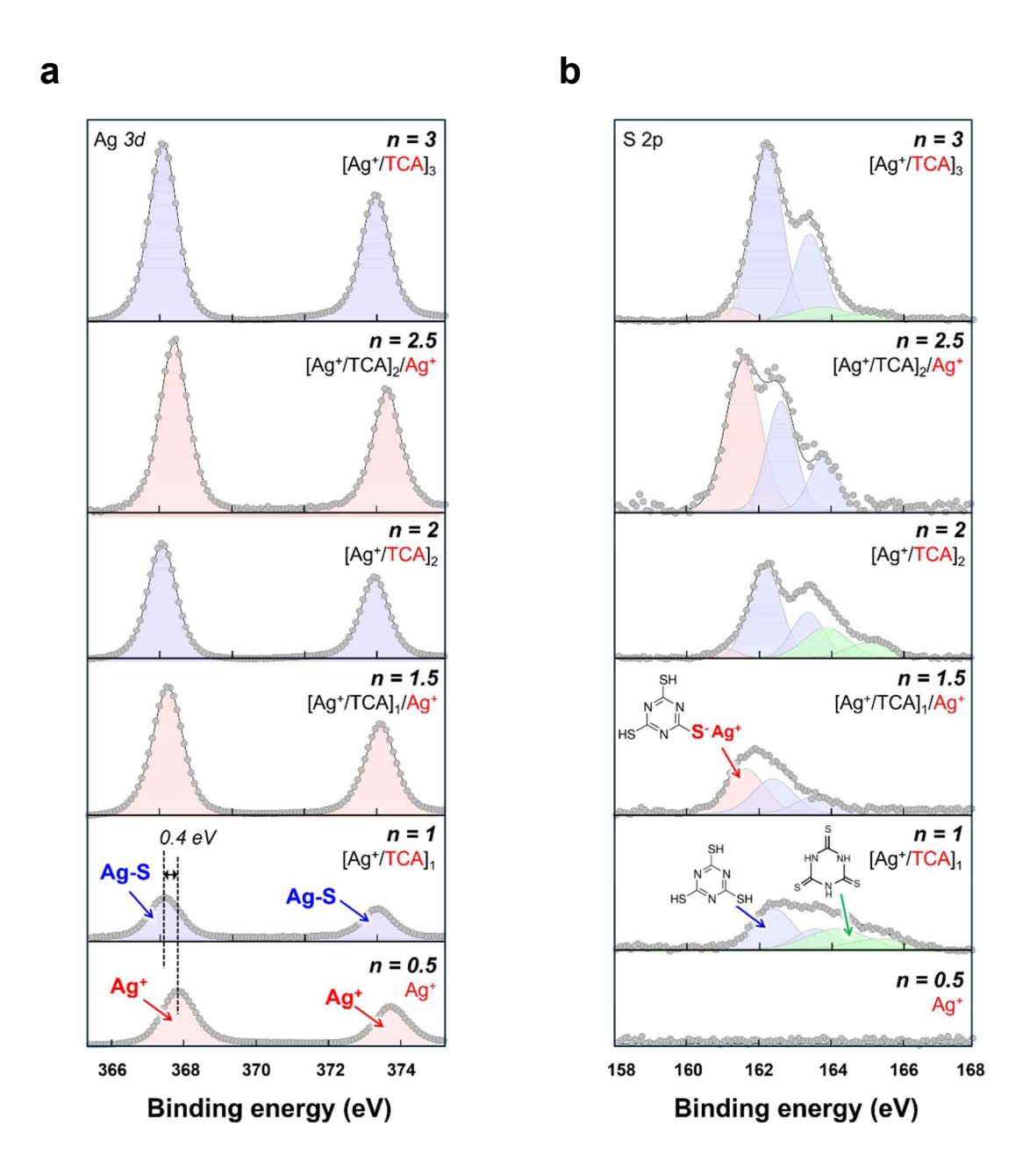


**Figure S5.** XPS spectra of (a) Ag 3d and (b) S 2p for [Ag<sup>+</sup>/TCA]<sub>n</sub>-MOF multilayers as a function of bilayer number (n). When Ag<sup>+</sup> ions were initially deposited onto a COOH-functionalized substrate, two distinct peaks were observed at 367.8 eV and 373.8 eV, corresponding to the Ag 3d<sub>5/2</sub> and Ag 3d<sub>3/2</sub> doublet of ionic Ag<sup>+</sup> (**Figure S5a**). Upon subsequent deposition of TCA, coordination bonding occurred via electron-donating sulfur atoms from the thiol groups in TCA, increasing the local electron density around Ag+. This resulted in a slight shift of the doublet to lower binding energies (~0.4 eV), now appearing at 367.4 eV and 373.4 eV—indicative of Ag–S coordination. After an additional Ag<sup>+</sup> deposition, the peaks shifted back by ~0.4 eV toward higher binding energies, reflecting the reappearance of Ag<sup>+</sup> as the

outermost layer. This alternating shift pattern was consistently observed with each successive deposition cycle, depending on whether the outermost layer was Ag<sup>+</sup> or TCA. The S 2p XPS spectra further supported this coordination behavior (**Figure S5b**). When TCA was the outermost layer (i.e., [Ag<sup>+</sup>/TCA]<sub>1</sub> bilayer), two sets of doublets were detected: one at 162.4 eV and 163.6 eV, corresponding to the S 2p<sub>3</sub>/<sub>2</sub>–2p<sub>1</sub>/<sub>2</sub> signals from the trithiol resonance form of TCA, and another at 164.2 eV and 165.4 eV, attributed to the trithione tautomer. Upon deposition of Ag<sup>+</sup> ions (i.e., [Ag<sup>+</sup>/TCA]<sub>1</sub>/Ag<sup>+</sup>), deprotonation of the thiol groups led to the formation of S<sup>-</sup>–Ag<sup>+</sup> coordination bonds, giving rise to a new S 2p doublet at 161.6 eV. Also, two peaks originating from the trithione tautomer disappeared, indicating that most of the TCA molecules interact with Ag<sup>+</sup> ions in a trithiol form. When TCA was further deposited onto Ag<sup>+</sup> ion-coated substrate (i.e., [Ag<sup>+</sup>/TCA]<sub>2</sub>), the characteristic peaks associated with the thiol and thione forms reappeared prominently. This trend repeated across the multilayers, confirming that Ag<sup>+</sup> ions and thiol groups in TCA consistently form coordination bonds at each interface.

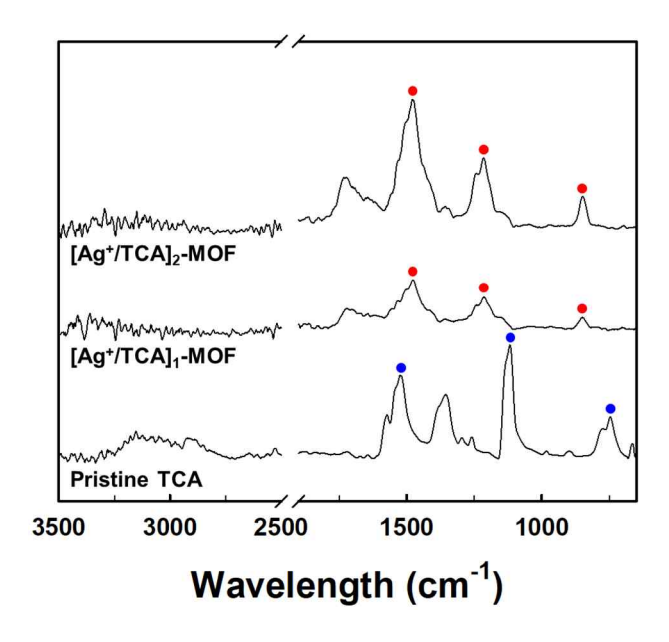


**Figure S6.** Fourier transform infrared spectroscopy (FTIR) spectra of pristine TCA molecule and [Ag<sup>+</sup>/TCA]<sub>n</sub>-MOF multilayers (n = 1 and 2). The pristine TCA showed distinct peaks at 1571, 1147, and 746 cm<sup>-1</sup>, corresponding to the nonaromatic trithione form of the triazine ring, along with a peak at 1357 cm<sup>-1</sup> and broad bands in the 2800-3300 cm<sup>-1</sup> region associated with N-H bending and stretching vibrations. On the other hand, the [Ag<sup>+</sup>/TCA]<sub>n</sub>-MOF exhibited prominent peaks at 1475, 1211, and 845 cm<sup>-1</sup>, which are characteristic of the aromatic trithiol form. These spectral changes indicate that the coordination between Ag<sup>+</sup> ions and donor atom (sulfur) in TCA induces a structural conversion from the nonaromatic trithione form to an aromatic trithiol form.

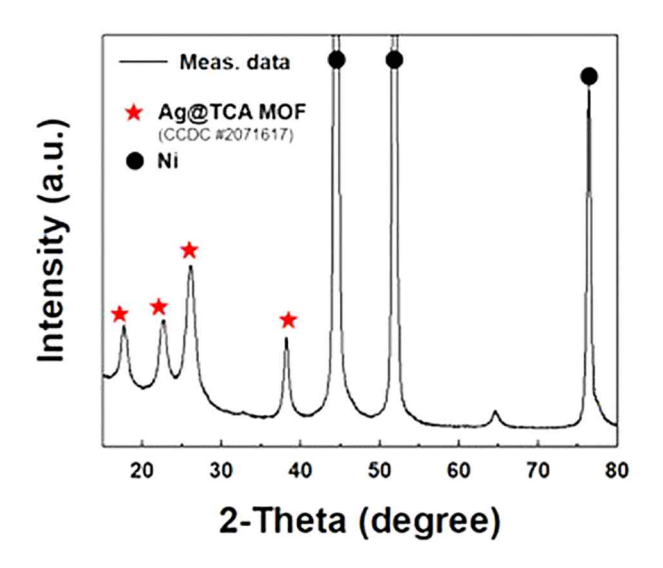


**Figure S7.** X-ray diffraction (XRD) patterns of  $[Ag^+/TCA]_n$ -MOF multilayers. the XRD patterns of the formed  $[Ag^+/TCA]_n$ -MOF multilayers showed distinct peaks at 17.6, 22.8, 26.1, and 38.2°, corresponding to the (110), (200), (211), and (222) crystal planes of MOF structure (note that the (222) plane may overlap with the Ag(111) reflection).

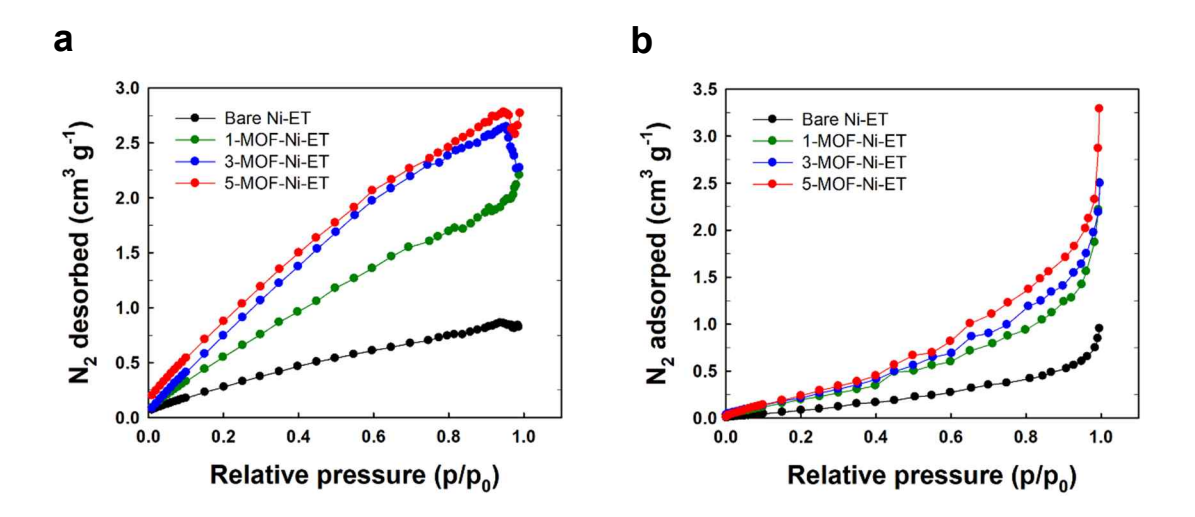


**Figure S8.**  $N_2$  (a) adsorption and (b) desorption isotherms of *n*-MOF-Ni-ET as a function of bilayer number.

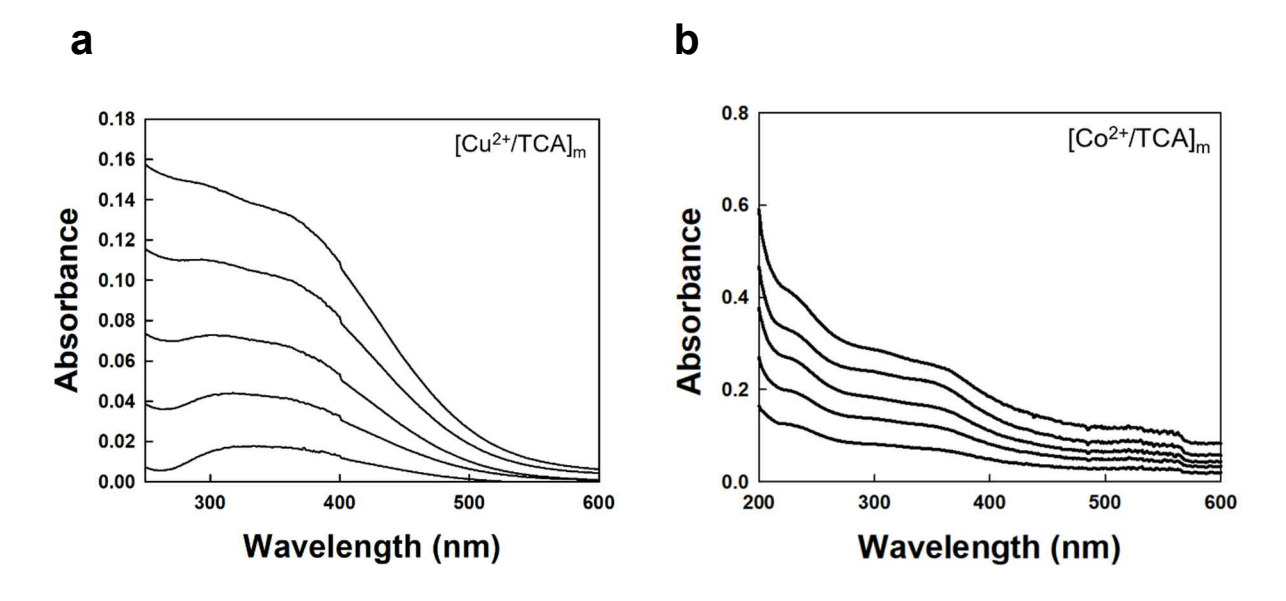


**Figure S9.** UV-vis absorbance spectra of (a)  $(Cu^{2+}/TCA)_m$ , and (b)  $(Co^{2+}/TCA)_m$  multilayers on quartz substrate with increasing bilayer number from 1 to 5.

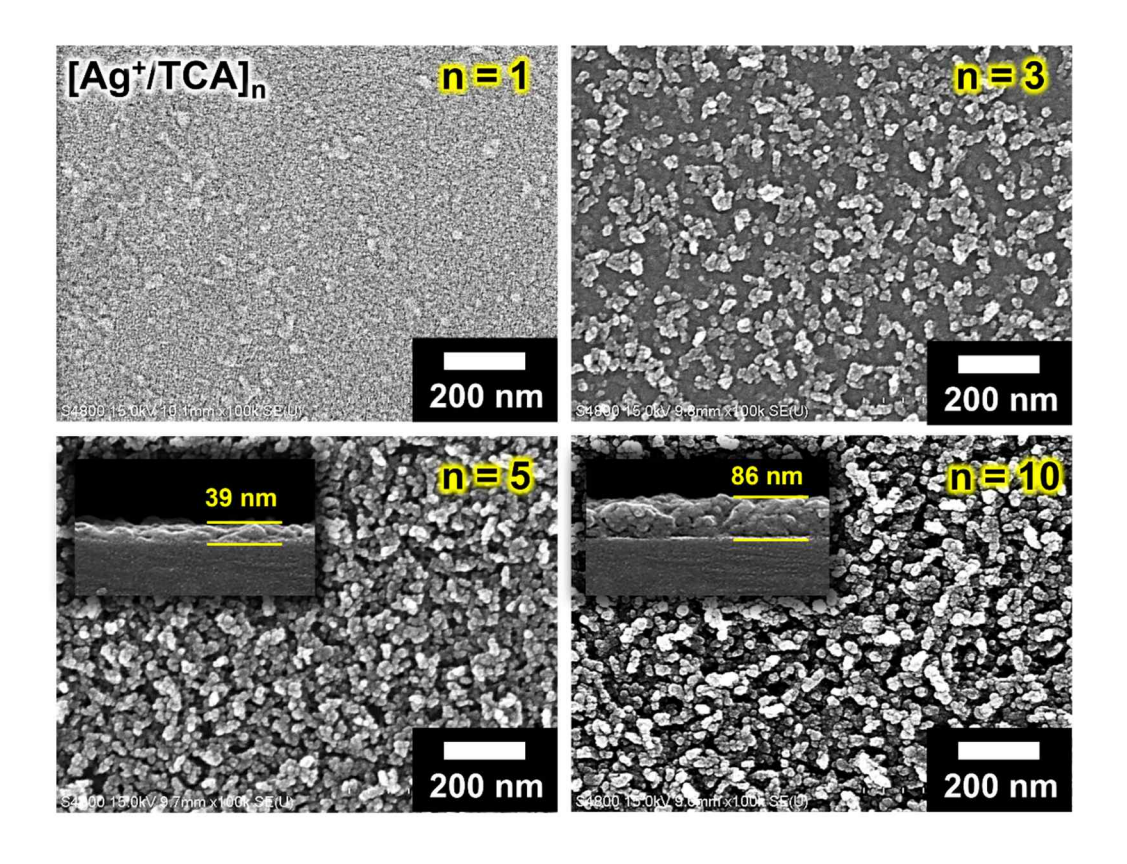


**Figure S10.** Planar and cross-sectional SEM images of [Ag<sup>+</sup>/TCA]<sub>n</sub>-MOF multilayers as a function of bilayer number (n).

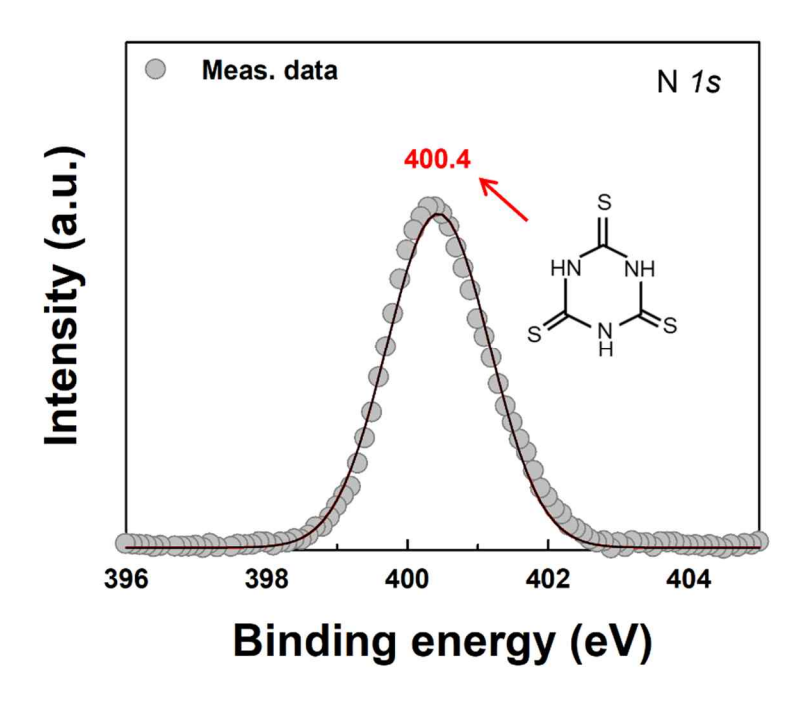


**Figure S11.** N 1s XPS spectrum of the TCA molecule. The samples were prepared by completely drying a drop-cast TCA solution on a substrate. The spectrum exhibited a single peak at 400.4 eV, corresponding to the C=N-C bond in the triazine ring structure.

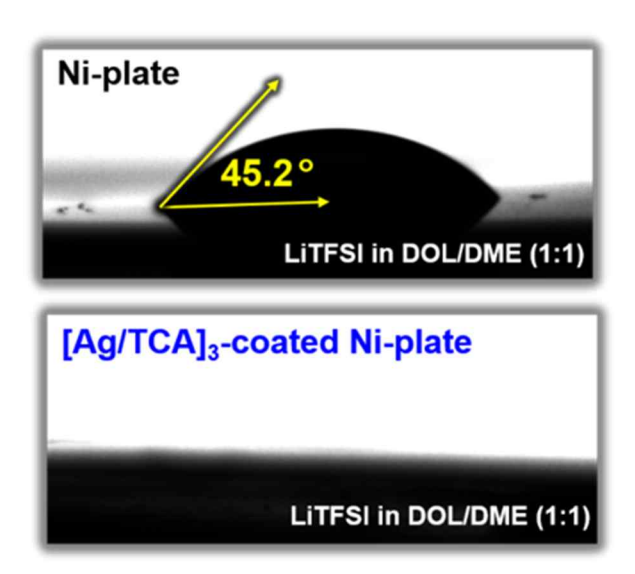


**Figure S12.** Electrolyte (1 M LiTFSI in DOL/DME (1:1) with 5 wt% LiNO<sub>3</sub>) contact angle measurements of bare Ni plate and [Ag<sup>+</sup>/TCA]<sub>n</sub>-MOF multilayer-coated Ni plates. As the bilayer number (n) of [Ag<sup>+</sup>/TCA]<sub>n</sub>-MOF multilayers increased, the contact angles gradually decreased, reaching complete wettability after 3 bilayers.

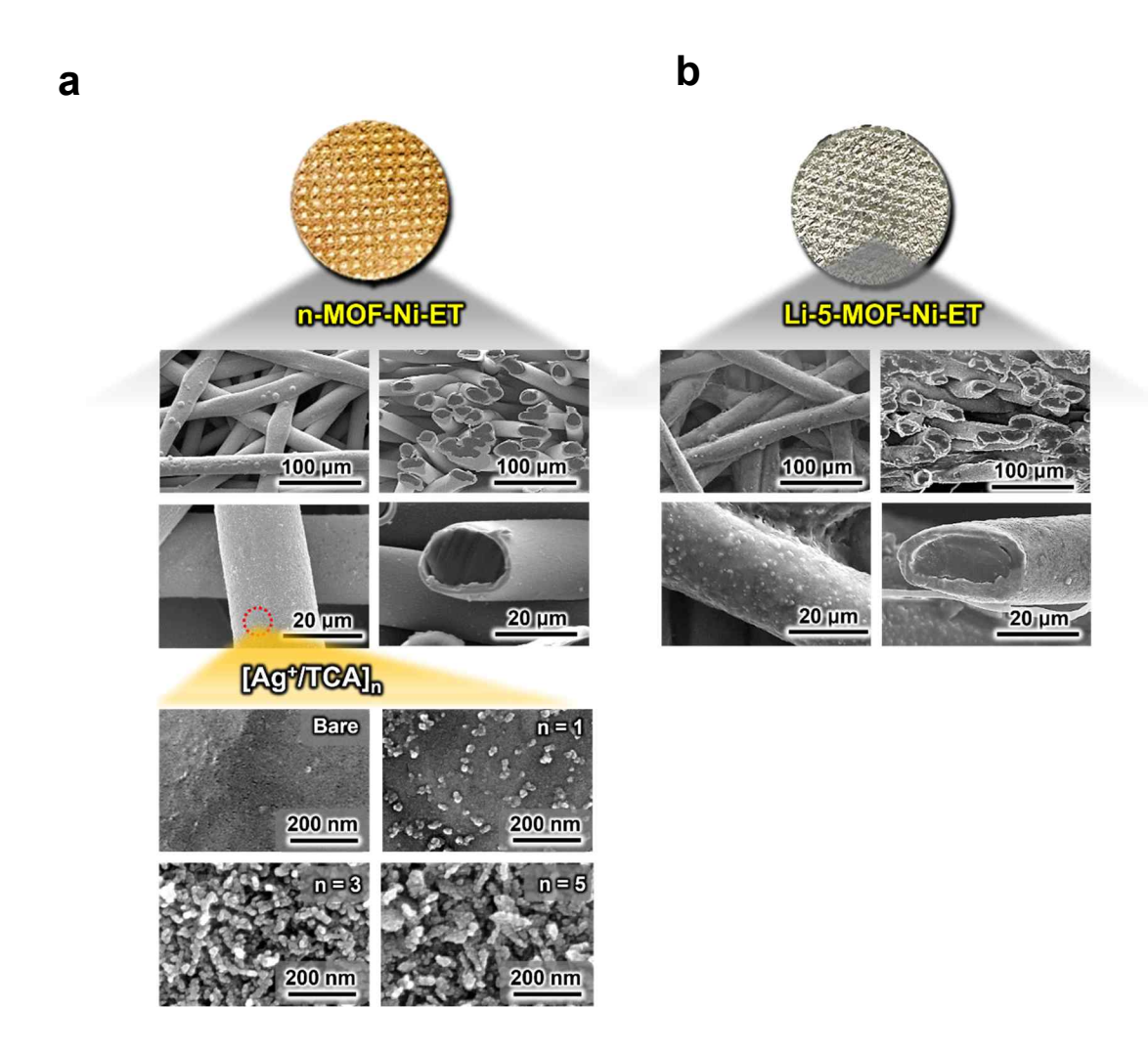


**Figure S13.** Digital and SEM images of (a) n-MOF-Ni-ET electrodes and (b) Li-5-MOF-Ni-ET.

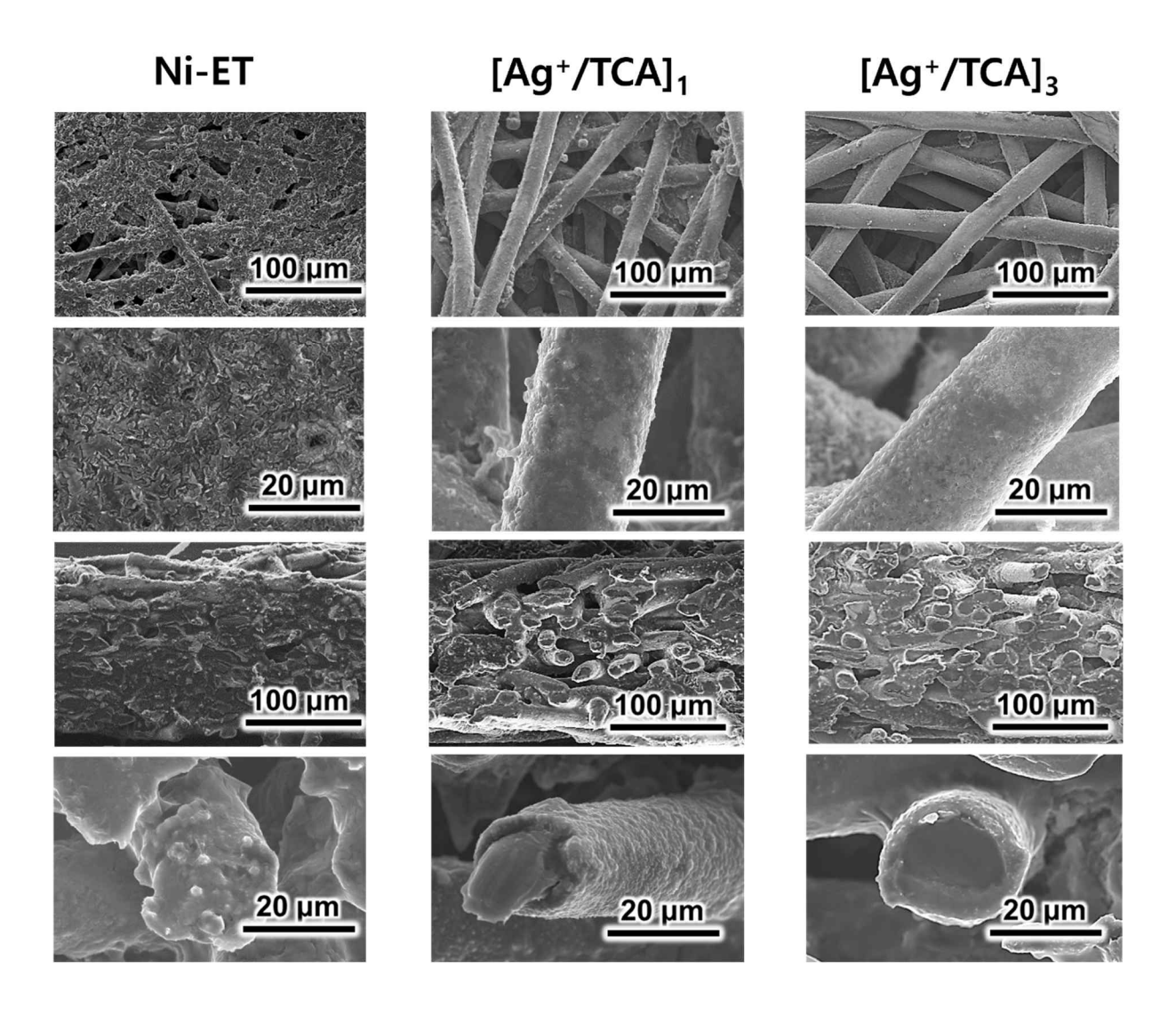
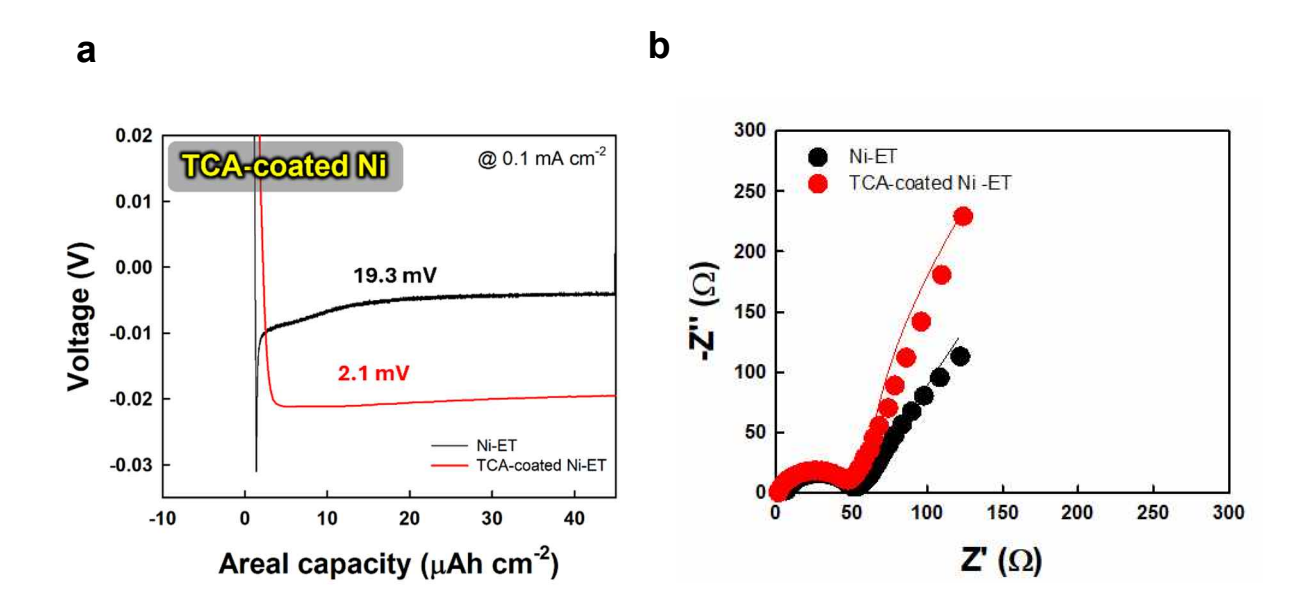
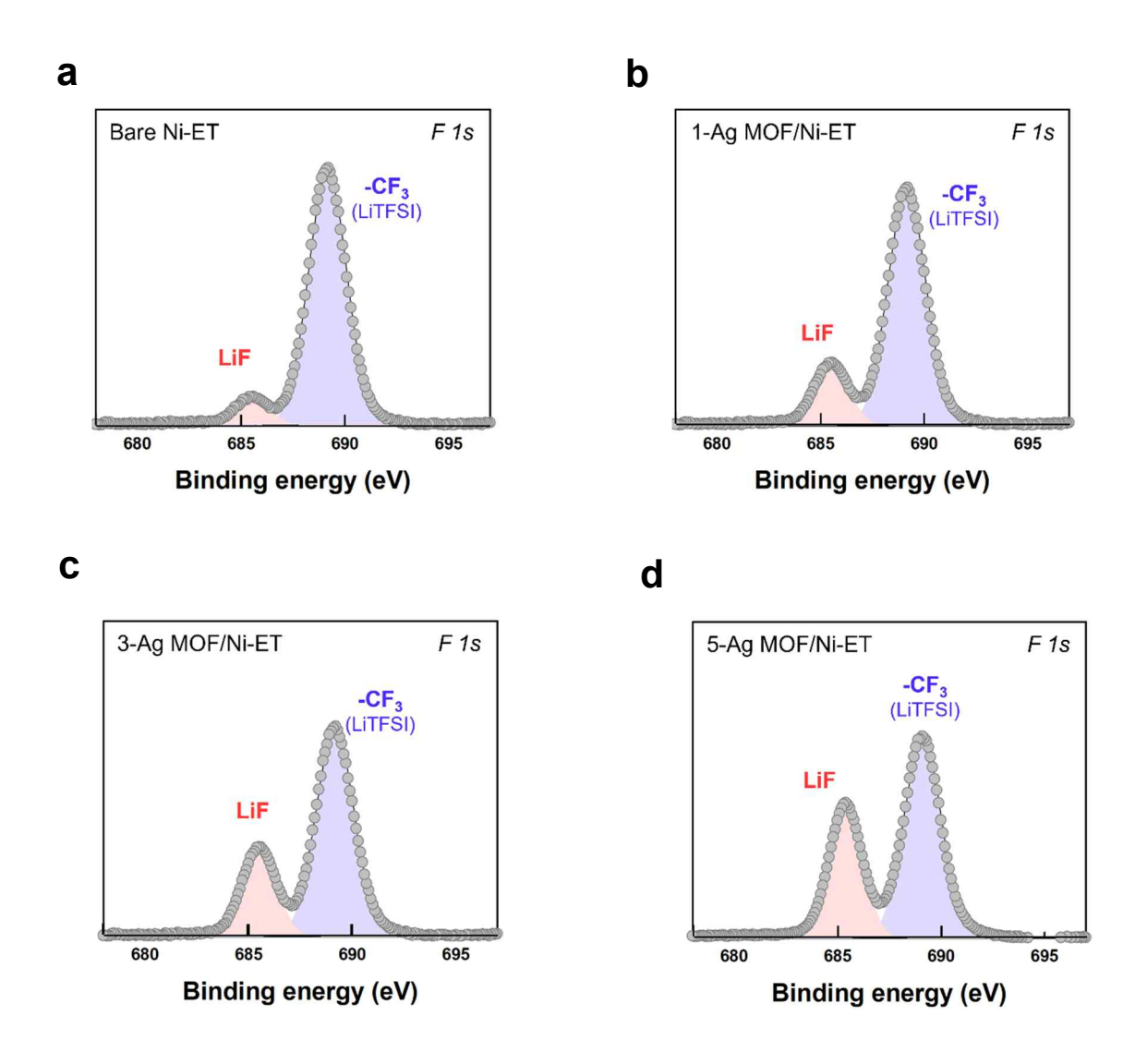


Figure S14. SEM images of n-MOF-Ni-ET (n = 0, 1, and 3) electrodes after Li plating.



**Figure S15.** (a) Voltage (V) *vs.* capacity (μAh cm<sup>-2</sup>) profiles and (b) Nyquist plots of TCA-coated Ni and bare Ni-electrode based half-cells during Li nucleation at 0.1 mA cm<sup>-2</sup> and 1 mAh cm<sup>-2</sup>. The TCA-coated Ni electrode exhibited a lithium nucleation overpotential of 2.1 mV during plating at 0.1 mA cm<sup>-2</sup> and 1 mAh cm<sup>-2</sup>, which is noticeably lower than that of the bare Ni electrode (19.3 mV). Furthermore, as shown in the Nyquist plots of each electrode, the TCA-Ni-ET also demonstrated a higher ionic conductivity of 5.8 mS cm<sup>-1</sup> compared to the bare Ni-ET (2.7 mS cm<sup>-1</sup>), indicating enhanced ion transport kinetics at the electrode interface, likely due to the formation of a more conductive SEI layer. These results clearly demonstrate that the TCA molecule plays a pivotal role in promoting the formation of a Li<sub>3</sub>N-rich SEI layer with both high ionic conductivity and mechanical robustness.



**Figure S16.** F 1s XPS spectrum of anion-dominant SEI layer on n-MOF-coated LTAs. (a) n = 0, (b) n = 1, (c) n = 3, and (d) n = 5.

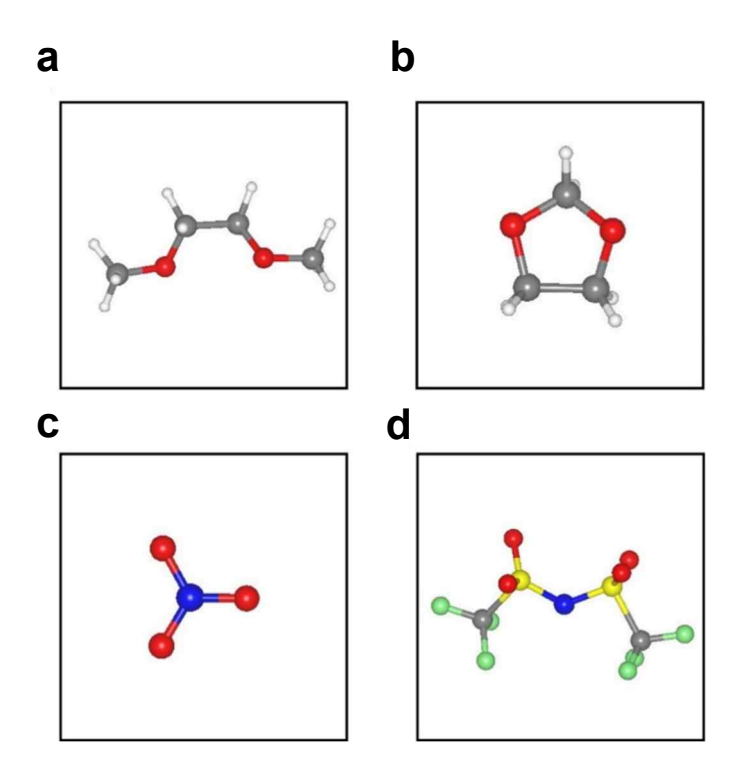


**Figure S17.** The structures of a) DME, b) DOL, c) NO<sub>3</sub><sup>-</sup>, and d) TFSI<sup>-</sup>. Color codes: red, (O), gray (C), light green (F), yellow (S), white (H) and blue (N).

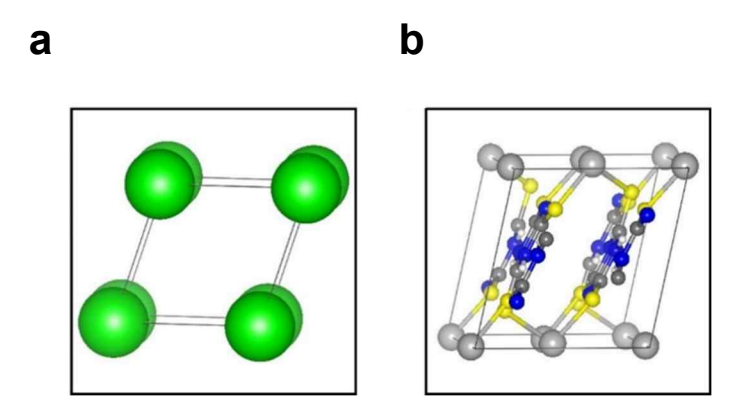


**Figure S18.** The bulk structures of (a) Ni and (b) [Ag<sup>+</sup>/TCA]<sub>n</sub>-MOF bulk. Color codes: red (O), gray (C), Silver (Au), yellow (S), white (H) and blue (N).

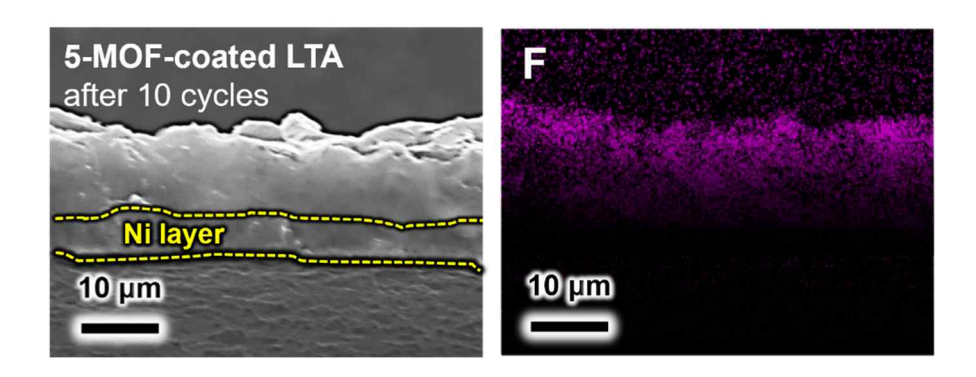


**Figure S19.** Cross-sectional SEM images and corresponding EDS elemental mapping of 5-MOF-coated LTAs.

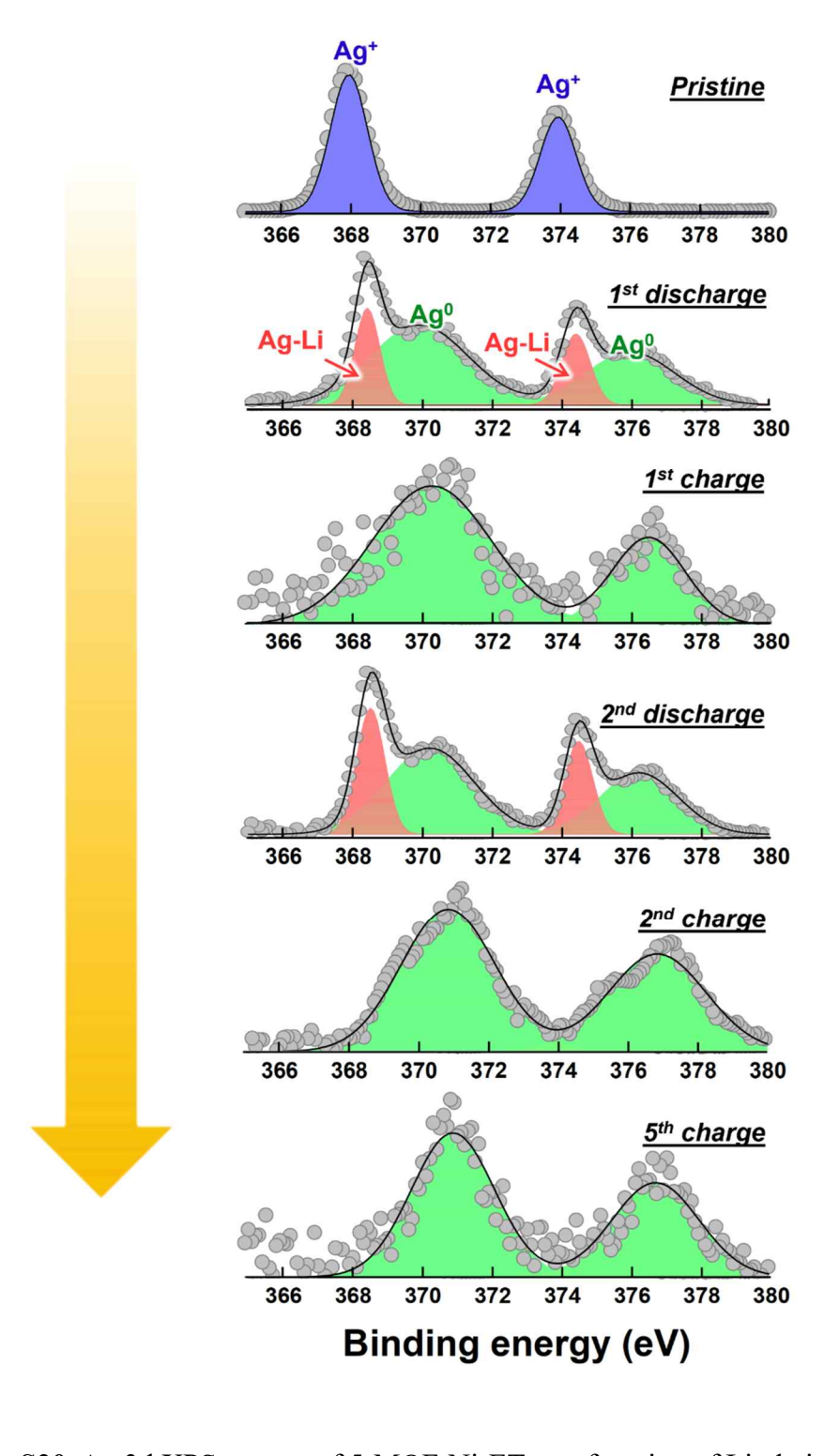
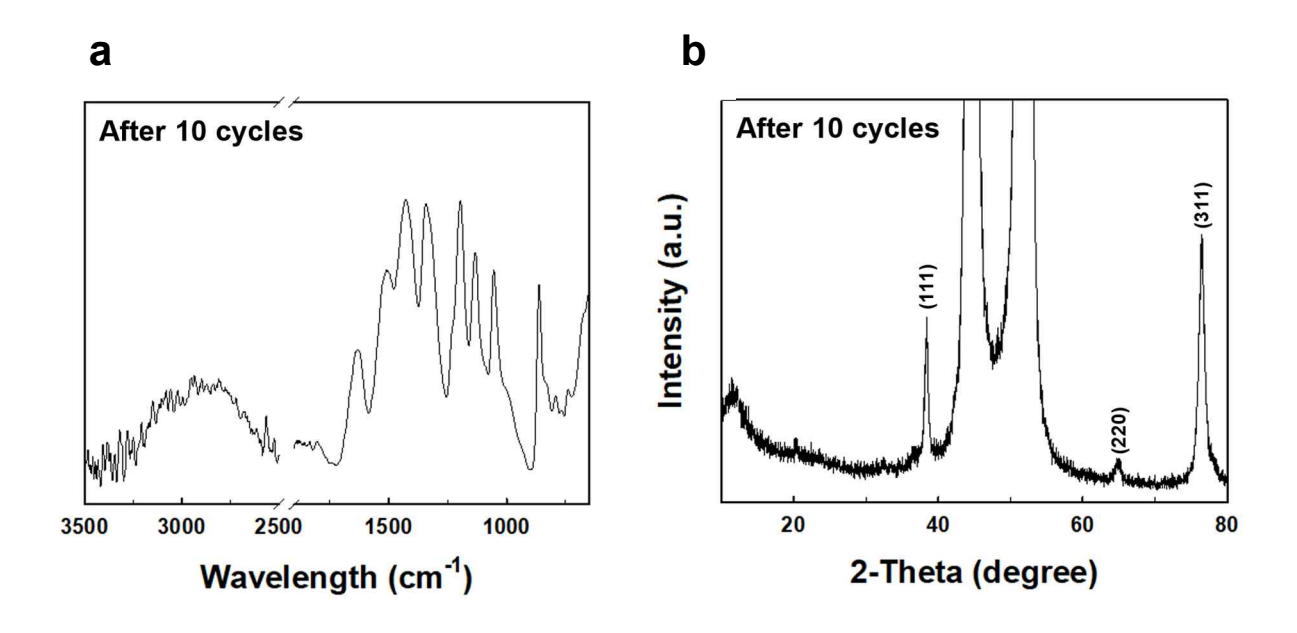
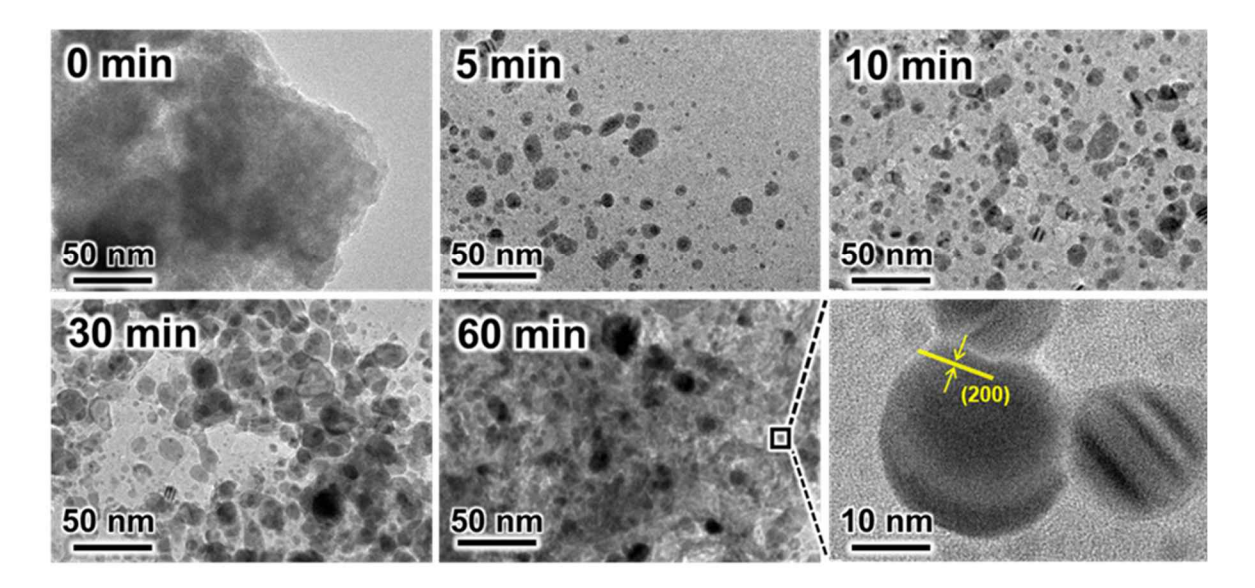


Figure S20. Ag 3d XPS spectra of 5-MOF-Ni-ET as a function of Li plating/stripping cycles.



**Figure S21.** (a) FTIR and (b) XRD spectra of [Ag<sup>+</sup>/TCA]<sub>n</sub>-MOF multilayers after electrochemical cycling. The characteristic vibrational modes of the [Ag<sup>+</sup>/TCA]<sub>n</sub>-MOF multilayers (observed in **Figure S6**) weaken and/or disappeared, and instead, several new peaks emerged: peaks at 1631, 1427, and 862 cm<sup>-1</sup> corresponding to carbonate species (e.g., Li<sub>2</sub>CO<sub>3</sub>); peaks at 1502 and 1342 cm<sup>-1</sup> attributed to nitrite/nitrate decomposition products from the LiNO<sub>3</sub>-containing electrolyte; and peaks at 1196, 1131, and 1055 cm<sup>-1</sup> assigned to ether-related C-O-C vibrations from DOL/DME solvent. Additionally, the XRD patterns of the [Ag<sup>+</sup>/TCA]<sub>n</sub>-MOF multilayer after cycling revealed new diffraction peaks at 64.4° and 77.5°, corresponding to the (220) and (311) planes of face-centered cubic (FCC) metallic Ag. This observation confirms that the Ag<sup>+</sup> ions within the MOF structure were effectively reduced to Ag NPs during repeated electrochemical cycling.

a



b

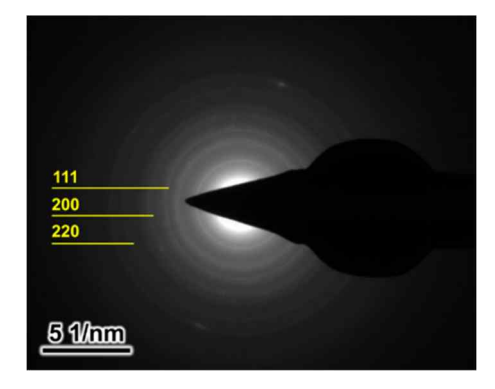


**Figure S22.** (a) HR-TEM images of [Ag<sup>+</sup>/TCA]<sub>5</sub>-MOF multilayers after lithium plating for 0 (bare), 5, 10, 30, and 60 min. (b) SAED pattern of [Ag<sup>+</sup>/TCA]<sub>5</sub>-MOF multilayers after lithium plating for 60 min. With increasing the plating time from 0 to 60 min, Ag NPs gradually emerged, eventually forming a densely distributed NP network after 60 min. Correspondingly, the electrode modified with [Ag<sup>+</sup>/TCA]<sub>5</sub>-MOF multilayer exhibited significantly improved cycling stability compared to the electrode without MOF, confirming that the presence of Ag NPs facilitates uniform lithium nucleation and effectively suppresses dendritic growth during repeated cycling.

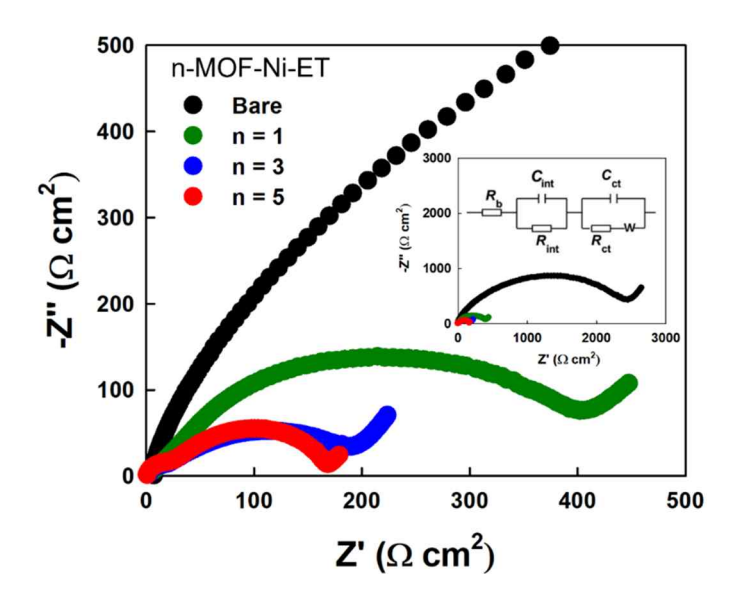


**Figure S23.** Nyquist plots of (Li//n-MOF-Ni-ET) half-cells with the bilayer number (n) ranging for 0 (bare Ni-ET) to 5 before cycling.

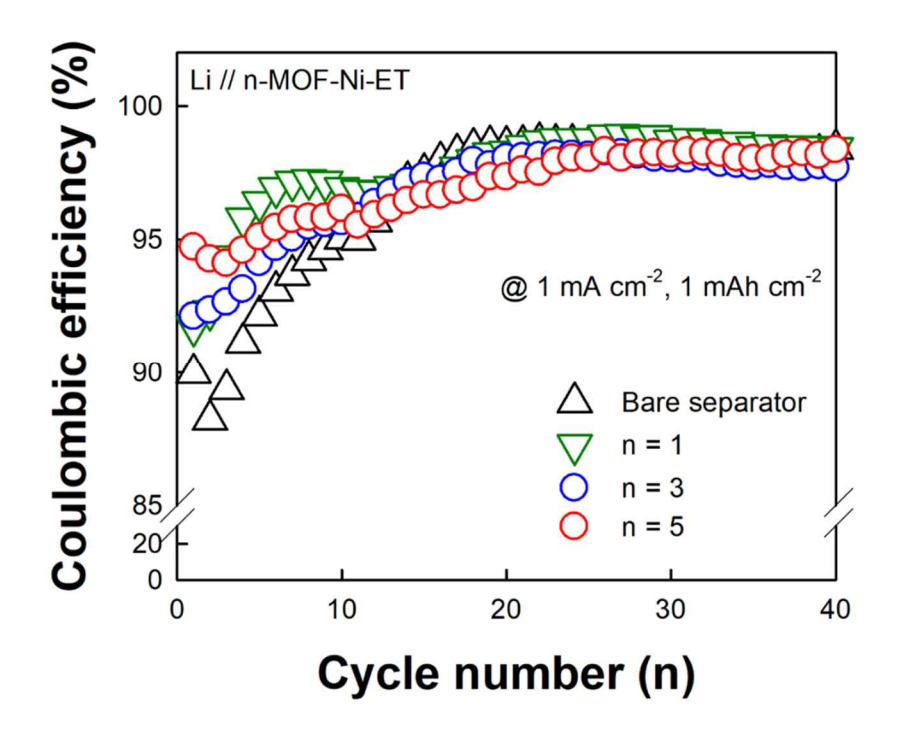


**Figure S24.** Changes in Coulombic efficiency (CE) values of (Li// n-MOF-Ni-ET) half-cells (n = 0, 1, 3, and 5) during the first 40 GCD cycles.

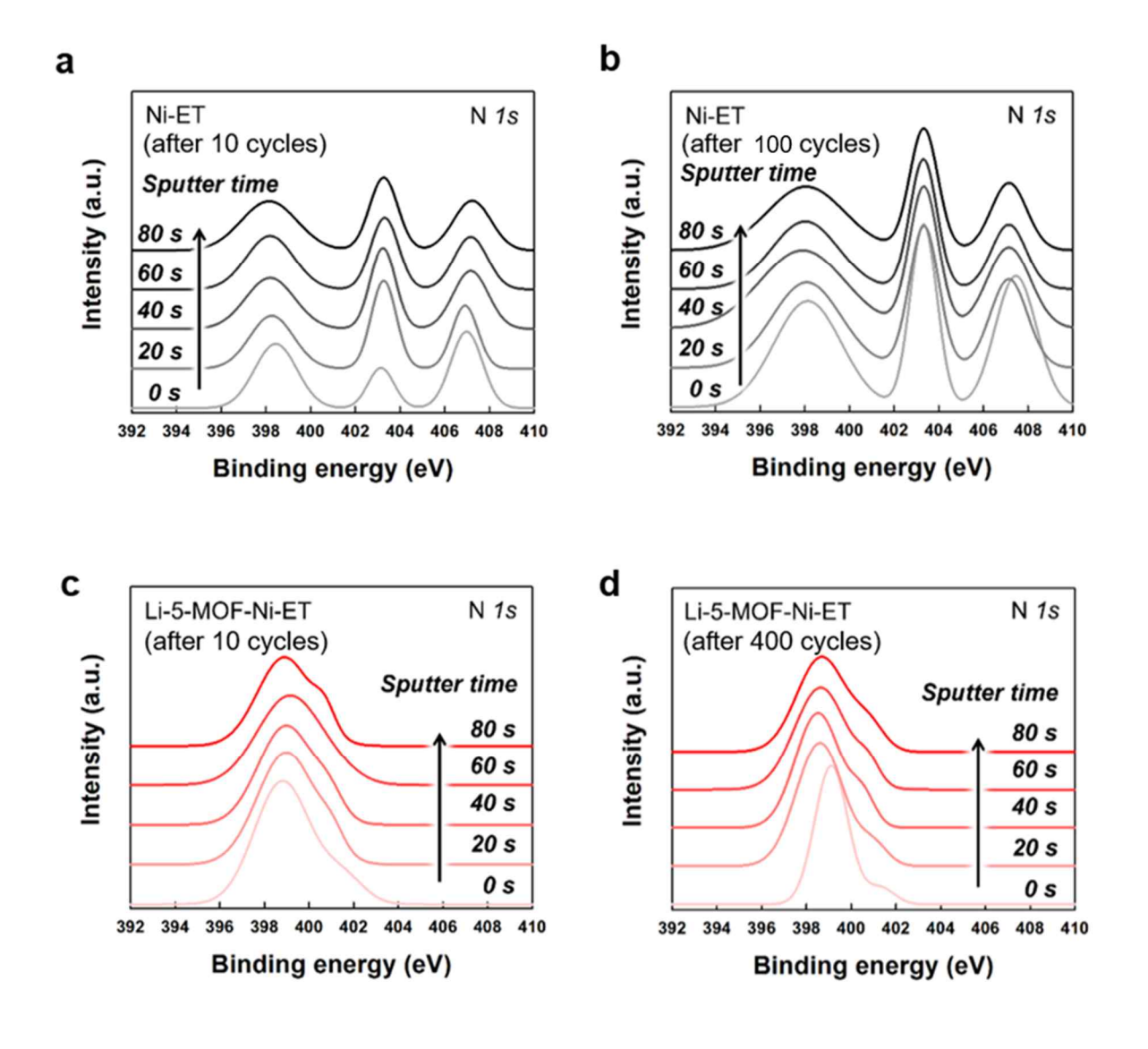


**Figure S25.** XPS depth profiles of bare Ni-ET-based half-cells after (a) 10 and (b) 100 cycles of Li plating/stripping, and Li-5-MOF-Ni-ET-based half-cells after (c) 10 and (d) 400 cycles of Li plating/stripping.

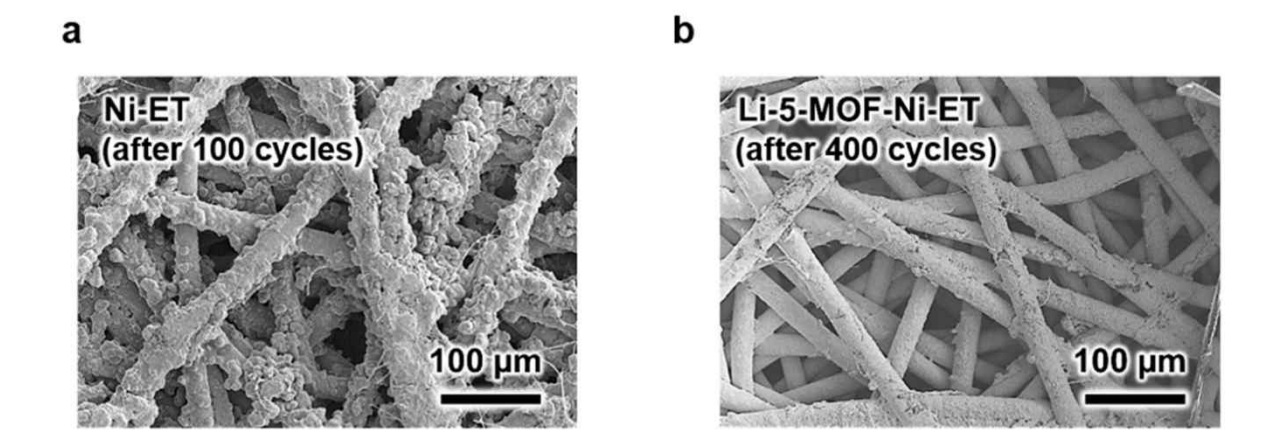


**Figure S26.** FE-SEM images of (a) bare Ni-ET and (b) Li-5-MOF-Ni-ET-based half-cells after GCD cycling at 1 mA cm<sup>-2</sup> and 1 mAh cm<sup>-2</sup>.

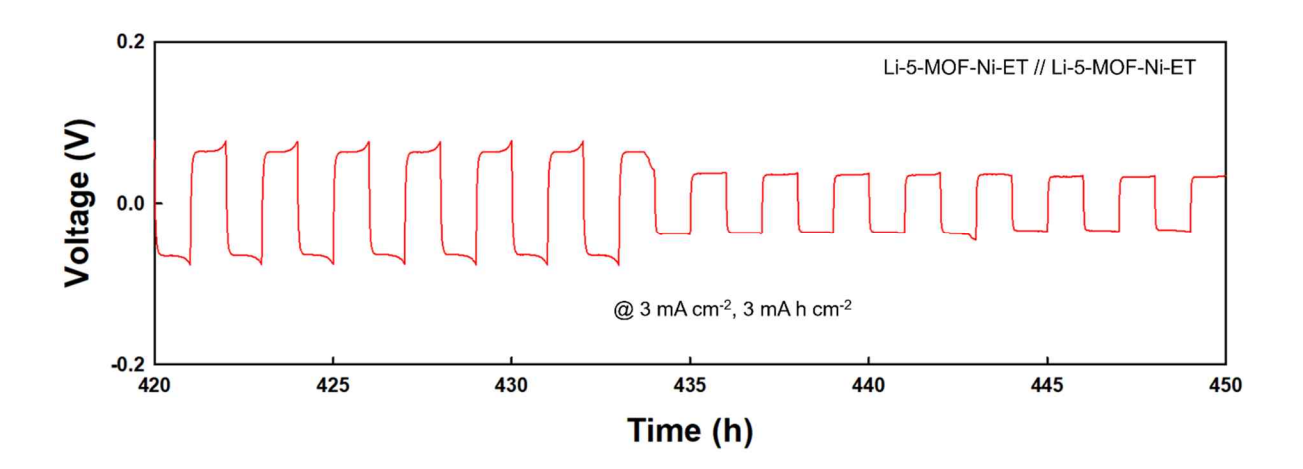


**Figure S27.** Enlarged view of the voltage profiles of Li-5-MOF-Ni-ET-based symmetric cell within the time window from 420 to 450 h in Figure 4g, highlighting the detailed overpotential behavior.

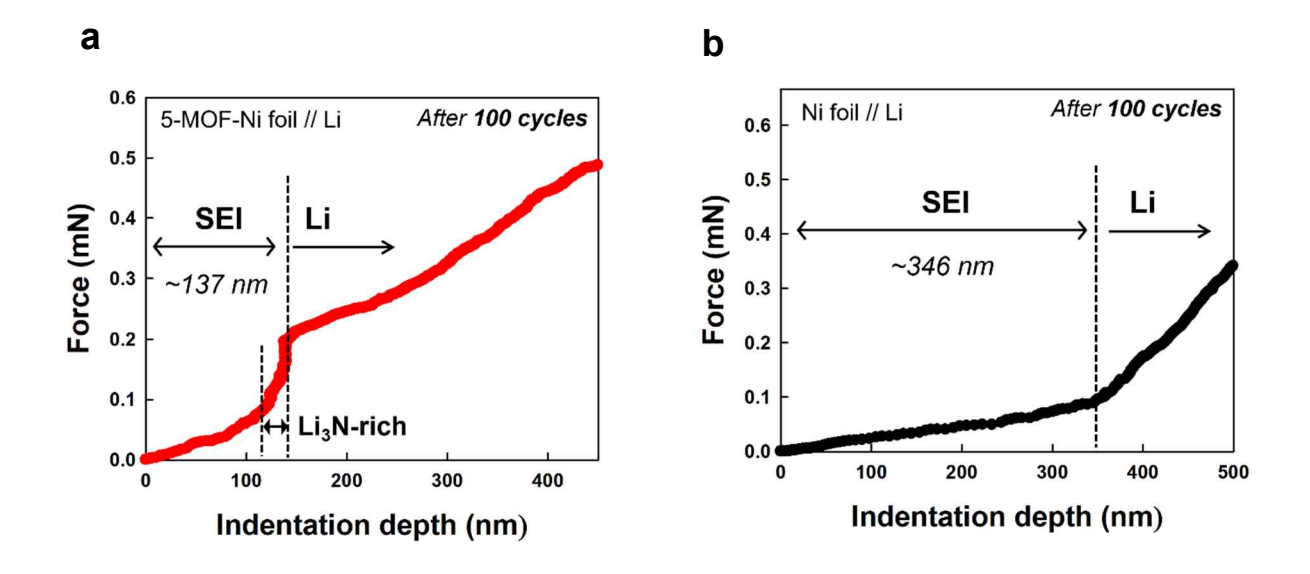


**Figure S28.** Typical force-indentation curves of (a) 5-MOF-Ni foil and (b) bare Ni foil electrodes after 100 plating/stripping cycles at 1 mA cm<sup>-2</sup> and 1 mAh cm<sup>-2</sup>. In this case, the nanoindentation analysis was performed using flat Ni foil as a host electrode instead of Ni-ET.

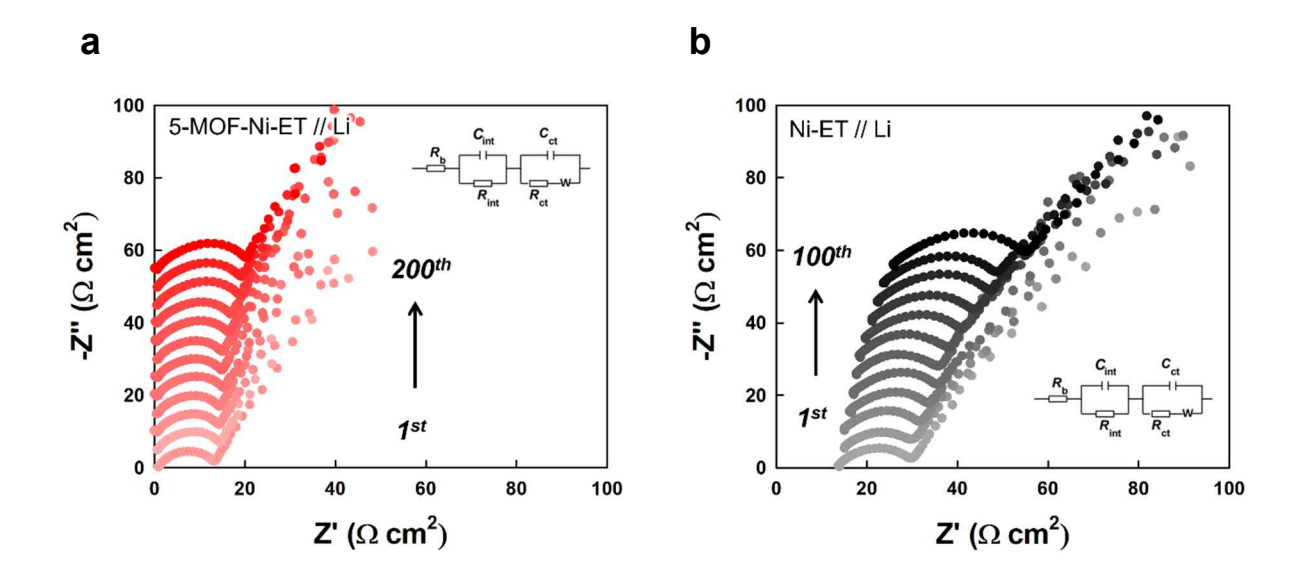


**Figure S29.** Nyquist plots of (a) Li-5-MOF-Ni-ET and (b) bare Ni-ET electrodes during electrochemical cycling at 1 mA cm<sup>-2</sup> and 1 mAh cm<sup>-2</sup>.

#### Specific capacity (mAh g<sup>-1</sup>) 0 20 100 120 140 160 3.8 Li-5-MOF-Ni-ET // LFP (16.7 mg cm<sup>-2</sup>) 3.6 3.9 V, N/P = 1.4 Voltage (V) 3.4 3.2 3.0 30<sup>th</sup> 60<sup>th</sup> 2.8 90<sup>th</sup> 110<sup>th</sup> 2.6 200<sup>th</sup> 2.4 1.5 2.0 0.5 1.0 2.5 0.0 3.0 Areal capacity (mAh cm<sup>-2</sup>)

**Figure S30.** Cycle number-dependent areal and specific capacities of (Li-5-MOF-Ni-ET//LFP) full-cells with an N/P ratio of 1.4.

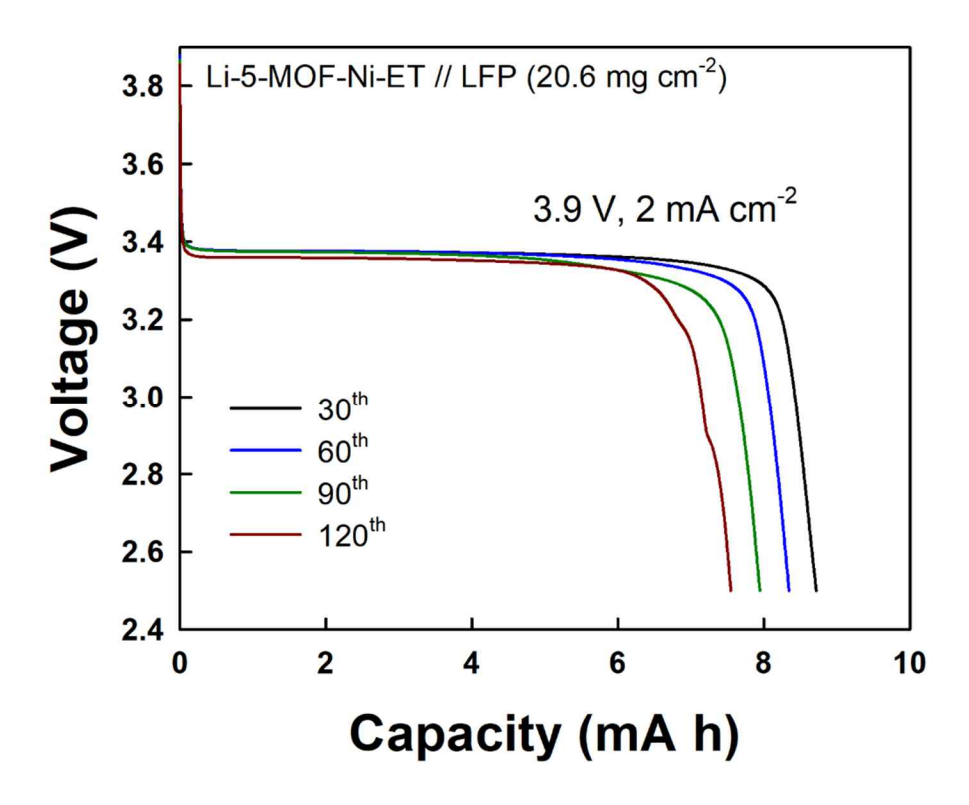


**Figure S31.** Cycle number-dependent areal and specific capacities of (Li-5-MOF-Ni-ET//LFP) pouch-cells with an N/P ratio of  $\sim$ 1.1.

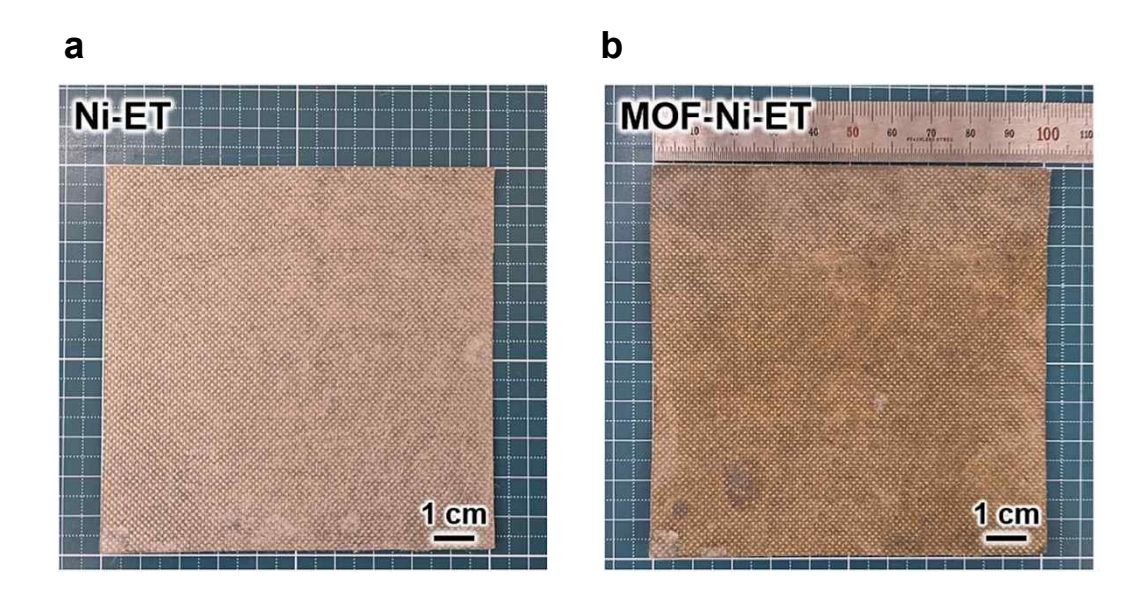


**Figure S32.** Photographic images of (a) Ni-ET and (b) MOF-Ni-ET samples with an area of  $10 \times 10 \text{ cm}^2$ .

MOF material	Method	Thickness	Mass loading	Li Li symmetric cell performance	Full cell performance	Full cell rate capability	Ref.
[Ag+/TCA] <sub>5</sub> -MOF	Layer-by-layer assembly	~39 nm	~3.5 ug cm-2	~2,000 h @1 mA cm- <sup>2</sup> /1 mAh cm- <sup>2</sup> 950 h @3 mA cm- <sup>2</sup> /3 mAh cm- <sup>2</sup>	LFP: 96.5% @1,300 cycles	65.2% @5 C	Our work
ZIF-8	Electrosynthesis	~1 µm	~20 µg cm-2	1800 h @2 mA cm-2/2 mAh cm-2	NCM811: 90.0% @400 cycles	-	[S18]
Ag-MOF	Hydrothermal	~5 µm	-	1000 h @0.5 mA cm <sup>-2</sup> /0.5 mAh cm <sup>-2</sup>	NCM811: 84.0% @350 cycles	72.8% @5 C	[S19]
Metal-azolate framework	Solvothermal	4.9 µm	-	2200 h @0.5 mA cm <sup>-2</sup> /1 mAh cm <sup>-2</sup> 600 h @1 mA cm <sup>-2</sup> /1 mAh cm <sup>-2</sup> 250 h @2 mA cm <sup>-2</sup> /1 mAh cm <sup>-2</sup>	LFP: 73.2% @1,500 cycles	~55.0% @3 C	[S20]
Ni-MOF	Solvothermal	~22 µm	-	150 h @1 mA cm <sup>-2</sup> /0.5 mAh cm <sup>-2</sup>	LFP: 98.1% @50 cycles	~71.0% @2 C	[S21]
MOF801	Hydrothermal	~30 µm	-	1,000 h @1 mA cm <sup>-2</sup> /1 mAh cm <sup>-2</sup>	LFP: 92.9% @500 cycles NCM811: @400 cycles	~79.2% @2 C	[S22]
ZIF-67	Hydrothermal	2.1 µm	-	500 h @1 mA cm-2/1 mAh cm-2	LFP: 96.3% @240 cycles	~71.6% @6 C	[S23]
NH <sub>2</sub> -MIL-125	Solvothermal	~10 µm	-	2000 h @1 mA cm <sup>-2</sup> /0.5 mAh cm <sup>-2</sup>	LFP: 87.4% @200 cycles	52.2% @2 C	[S24]
ZIF-8	Electrodeposition	8 µm	40 μg cm- <sup>2</sup>	500 h @1mA cm <sup>-2</sup> /2 mAh cm <sup>-2</sup>	LFP: 84.6% @500 cycles	70.0% @1 C	[S25]

**Table S1.** Comparison of the electrochemical performance of our [Ag+/TCA]n-MOF-Ni-ET anode with previously reported LMAs incorporated MOF-modified separators.

Electrode	Li loading (mAh cm <sup>-2</sup> )	Specific anode capacity (mAh g-1)	Ref.
5-MOF-Ni-ET	4	~100	Our work
5-MOF-Ni-ET	50	~1000	Our work
In <sub>3</sub> Li <sub>13</sub> @NF	4	~82.3	[S26]
3DLCC	6	~128.8	[S27]
3DMN Cu	7.87	~94.8	[S28]
Cu-mesh CC	4	~428.4	[S29]

**Table S2.** Comparison of the specific anode capacity of our 5-MOF-Ni-ET anode with previously reported LMAs.

#### **Supplementary References**

- [S1] M. Brust, M. Walker, D. Bethell, D. J. Schiffrin, R. Whyman, Synthesis of thiol-derivatised gold nanoparticles in a two-phase Liquid-Liquid system. J. Chem. Soc., Chem. Commun. 1994, 7, 801–802.
- [S2] G. Kresse, J. Hafner, Ab initio molecular dynamics for liquid metals. *Phys. Rev. B* **1993**, 47, 558–561.
- [S3] G. Kresse, J. Furthmüller, Efficiency of ab-initio total energy calculations for metals and semiconductors using a plane-wave basis set. *Comput. Mater. Sci.* **1996**, *6*, 15–50.
- [S4] J. P. Perdew, K. Burke, M. Ernzerhof, Generalized gradient approximation made simple. *Phys. Rev. Lett.* **1996**, 77, 3865–3868.
- [S5] G. Kresse, D. Joubert, From ultrasoft pseudopotentials to the projector augmented-wave method. *Phys. Rev. B* **1999**, *59*, 1758–1775.
- [S6] P. E. Blöchl, Projector augmented-wave method. *Phys. Rev. B* **1994**, *50*, 17953–17979.
- [S7] S. Grimme, S. Ehrlich, L. Goerigk, Effect of the damping function in dispersion corrected density functional theory. *J. Comput. Chem.* **2011**, *32*, 1456–1465.
- [S8] H. J. Monkhorst, J. D. Pack, Special points for Brillouin-zone integrations. *Phys. Rev. B* **1976**, *13*, 5188–5192.
- [S9] R. Sundararaman, W. A. Goddard, T. A. Arias, Grand canonical electronic density-functional theory: Algorithms and applications to electrochemistry. *J. Chem. Phys.* **2017**, *146*, 114104.
- [S10] K. Mathew, R. Sundararaman, K. Letchworth-Weaver, T. Arias, R. G. Hennig, Implicit solvation model for density-functional study of nanocrystal surfaces and reaction pathways. *J. Chem. Phys.* **2014**, *140*, 084106.
- [S11] K. Mathew, V. C. Kolluru, R. Hennig, VASPsol: Implicit solvation and electrolyte model for density-functional theory. Available online: https://github.com/henniggroup/VASPsol (2018).

- [S12] W. Wu, Y. Zhang, Y. Guo, J. Bai, C. Zhang, Z. Chen, Y. Liu, B. Xiao, Exploring anchoring performance of InP<sub>3</sub> monolayer for lithium-sulfur batteries: A first-principles study. *Appl. Surf. Sci.* **2020**, *526*, 146717.
- [S13] J. Wang, X. Jia, L. Bai, X. Qu, Two-dimensional SnP<sub>3</sub> monolayer for inhibiting the shuttle effect in lithium-sulfur batteries: A first-principles study. *Comput. Mater. Sci.* 2024, 241, 113041.
- [S14] S. Trasatti, The absolute electrode potential: an explanatory note (Recommendations 1986). *Pure Appl. Chem.* **1986**, *58*, 955–966.
- [S15] F. H. Allen, M. D. Bellard, B. A. Brice, A. D. Cartwright, H. Higgs, T. Hummelink, B. G. Hummelink-Peter, O. Kennard, W. D. S. Motherwell, J. R. Rogers, D. G. Watson, The Cambridge Crystallographic Data Centre: computer-based search, retrieval, analysis and display of information. *Acta Crystallogr. Sect. B* 1979, 35, 2331–2339.
- [S16] T. Wakiya, Y. Kamakura, H. Shibahara, K. Ogasawara, A. Saeki, R. Nishikubo, A. Inokuchi, H. Yoshikawa, D. Tanaka, Machine-learning-assisted selective synthesis of a semiconductive silver thiolate coordination polymer with segregated paths for holes and electrons. *Angew. Chem. Int. Ed.* 2021, 60, 23080–23087.
- [S17] Y. Fan, R. Li, R. Yi, L. Zheng, J. Wang, R. Huang, Z. Gong, Z. Li, J. Qi, X. Liu, X. Fan, Y. Shen, L. Chen, Surface-dipole-directed formation of stable solid electrolyte interphase. *Cell Rep. Phys. Sci.* 2023, 4, 101324.
- [S18] Z. Chang, H. Yang, A. Pan, P. He, H. Zhou, An improved 9 micron thick separator for a 350 Wh/kg lithium metal rechargeable pouch cell. *Nat. Commun.* **2022**, *13*, 6788.
- [S19] L.-Y. Yang, J. H. Cao, W. H. Liang, Y.-K. Wang, D.-Y. Wu, Effects of the separator MOF-Al<sub>2</sub> O<sub>3</sub> coating on battery rate performance and solid–electrolyte interphase formation. *ACS Appl. Mater. Interfaces* **2022**, *14*, 13722–13732.
- [S20] W.-L. Wu, Y.-T. Xu, X. Ke, Y.-M. Chen, Y.-F. Cheng, G.-D. Lin, M.-P. Fan, L.-Y. Liu, Z.-C. Shi, Superorganophilic MAF-6/PP composite separator boosts lithium metal battery performance. *Energy Storage Mater.* **2021**, *37*, 387–395.

- [S21] Z. Hao, Y. Wu, Q. Zhao, J. Tang, Q. Zhang, X. Ke, J. Liu, Y. Jin, H, Wang, Functional separators regulating ion transport enabled by metal-organic frameworks for dendrite-free lithium metal anodes. *Adv. Funct. Mater.* **2021**, *31*, 2102938.
- [S22] L. Zuo, Q. Ma, P. Xiao, Q. Guo, W. Xie, D. Lu, X. Yun, C. Zheng, Y. Chen, Upgrading the separators integrated with desolvation and selective deposition toward the stable lithium metal batteries. *Adv. Mater.* **2024**, *36*, 2311529.
- [S23] G. Lin, K. Jia, Z. Bai, C. Liu, S. Liu, Y. Huang, X. Liu, Metal-organic framework sandwiching porous super-engineering polymeric membranes as anionphilic separators for dendrite-free lithium metal batteries. *Adv. Funct. Mater.* **2022**, *32*, 2207969.
- [S24] F. Zhu, J. Wang, Y. Zhang, H. Tu, X. Xia, J. Zhang, H. He, H. Lin, M. Liu, Low-temperature lithium metal batteries achieved by synergistically enhanced screening Li<sup>+</sup> desolvation kinetics. *Adv. Mater.* **2025**, *37*, 2411601.
- [S25] X. Lin, R. Baranwal, G. Ren, Z. Fan, Cathodically deposited ZIF-8 compact layer on an 8-μm ultrathin polypropylene separator to enhance the performance of lithium-sulfur and lithium-metal batteries, *Chem. Eng. J.* **2024**, *500*, 157192.
- [S26] Y. Fan, J. Liao, D. Luo, Y. Huang, F. Sun, J. Nam, In situ formation of a lithiophilic surface on 3D current collectors to regulate lithium nucleation and growth for dendrite-free lithium metal anodes, *Chem. Eng. J.* **2023**, *453*, 139903.
- [S27] C. Guo, Y. Guo, R. Tao, X Liao, K. Du, H. Zou, W. Zhang, J. Liang, D. Wang, X.-G. Sun, S.-Y. Lu, Uniform lithiophilic layers in 3D current collectors enable ultrastable solid electrolyte interphase for high-performance lithium metal batteries, *Nano Energy* 2022, 96, 107121.
- [S28] I. Yang, J.-H. Jeoung, J. Y. Weok, S. Kim, Structurally tailored hierarchical Cu current collector with selective inward growth of lithium for high-performance lithium metal batteries, *Adv. Energy. Mater.* **2023**, *13*, 2202321.
- [S29] D. Li, Y. He, B. Chen, J. Xu, Q. Liu, S. Yang, W.-Y. Lai, Self-smoothing lithium metal anode based on screen-printed Cu-mesh current collector for long-term safety of lithium metal batteries, *Eco Energy* **2024**, *3*, 311-321.